2017

Utilizing Structure-From-Motion Photogrammetry and Unmanned Aerial Vehicles to Characterize Variability in Fluvial Deposits from the Salt Wash Member of the Morrison Formation, East-Central Utah

John Chesley
University of South Carolina

Utilizing Structure-from-Motion photogrammetry and Unmanned aerial vehicles to characterize variability in fluvial deposits from the Salt Wash Member of the Morrison Formation, east-central Utah

by

John Chesley

Bachelor of Science
University of Northern Iowa, 2014

Submitted in Partial Fulfillment of the Requirements

For the Degree of Master of Science in

Geological Sciences

College of Arts and Sciences

University of South Carolina

2017

Accepted by:

Andrew Leier, Director of Thesis

David Barbeau, Reader

Scott White, Reader

Cheryl L. Addy, Vice Provost and Dean of the Graduate School

DEDICATION

I would like to dedicate this thesis to my parents, Susan and Steve Chesley.

ACKNOWLEDGEMENTS

This research was partly funded by the Lauren A. Wright & Bennie Troxel Student Research Award through GSA and the Gordon I. Atwater Memorial Grant through AAPG. I would like to extend my thanks to my advisor, Andrew Leier for his help and encouragement. Thank you to my committee members, Scott White and David Barbeau, for their helpful advice and suggestions. Dr. Ray Torres for helping me collect ground control point data. Thank you to Cody Heinze for his assistance in collecting the data. I would like to acknowledge Christina Maschmeyer and Douglas Cahl for their helpful suggestions and advice.

ABSTRACT

Modern fluvial systems are highly variable, often containing the entire spectrum of fluvial styles (e.g., braided to meandering). This variability is difficult to capture in ancient fluvial deposits due to limited 1- and 2-dimesional exposures, which provide only a snapshot of the depositional history at one location. As a result, researchers are forced to interpolate between exposures and develop regional scale models that often underestimate the complexity and variability seen in modern environments. Outcrops of the Upper Jurassic Salt Wash Member of the Morrison Formation in east-central Utah, USA provide a relatively unique opportunity to examine ancient fluvial sandstone bodies in planview. However, capturing the 3-dimensional nature of these outcrops is problematic in that field-based observations are too specific to delineate larger-scale trends, and existing aerial imagery does not have the resolution to distinguish important details. This thesis outlines the workflow and results of a study that utilizes unmanned aerial vehicles (UAV) and structure-from-motion (SfM) photogrammetry to produce sub-meter-scale outcrop reconstructions in 3-D. Overall, average values of sandstone body characteristics (width, orientation, paleocurrent, etc.) in the Salt Wash Member are consistent with existing models. However, within this spectrum are four distinct types of fluvial deposits, each with its own characteristics. Very narrow sandstone bodies (4-6 m wide) occur in

groups, are less than 2 m thick and heavily bioturbated. Narrow sandstone bodies (15 to 45 m wide) are straight to sinuous, contain evidence of lateral migration, and were deposited by east-northeast flowing fluvial systems. Medium sandstone bodies (75 to 105 m wide) are straight, and were deposited by non-migrating, east-flowing fluvial systems. Sheet/other sandstone bodies consist of both sheet-like sandstones whose edges are not visible and eroded sandstones bodies that cannot be reconstructed. The succession is consistent with a distributive fluvial system model (DFS) previously proposed for the Salt Wash Member. However, the variability of sandstone bodies and orientations in this area suggest these deposits may be more variable at local scales (e.g. 10km^2) than what would be predicted by existing DFS models.

TABLE OF CONTENTS

DEDICATION iii

ACKNOWLEDGEMENTS iv

ABSTRACT v

LIST OF TABLES viii

LIST OF FIGURES ix

LIST OF ABBREVIATIONS xi

CHAPTER 1: INTRODUCTION 1

CHAPTER 2: LITERATURE REVIEW 6

CHAPTER 3: USING UNMANNED AERIAL VEHICLES AND STRUCTURE-FROM-MOTION PHOTOGRAMMETRY TO CHARACTERIZE SEDIMENTARY OUTCROPS: AN EXAMPLE FROM THE MORRISON FORMATION, UTAH, USA 13

CHAPTER 4: PLANVIEW VARIABILITY OF FLUVIAL DEPOSITS IN THE SALT WASH MEMBER OF THE MORRISON FORMATION, EAST-CENTRAL UTAH 36

CHAPTER 5: CONCLUSION 85

REFERENCES 87

APPENDIX A: UAV-SFM ACCURACY ASSESSMENT 97

LIST OF TABLES

Table 4.1 Paleohydraulic equations and calculations 82

Table A.1 Summary of datasets used in the accuracy assessment and case study..... 102

Table A.2 Results from the one-way ANOVA test..... 103

LIST OF FIGURES

Figure 3.1 SfM photogrammetry schematic diagram 27

Figure 3.2 Unmanned aerial vehicle examples 28

Figure 3.3 SfM concept & processing 29

Figure 3.4 Study area 30

Figure 3.5 SfM data acquisition and models 31

Figure 3.6 Comparison between UAV-SfM data & GoogleEarth™ 32

Figure 3.7 Interpreted orthomosaic & DSM 33

Figure 3.8 Orthomosaic measurements at different scales 34

Figure 3.9 Volumetric and area calculations 35

Figure 4.1 Stratigraphy of the Morrison Formation and extent of the Salt Wash Member 67

Figure 4.2 Study area 68

Figure 4.3 SfM concept 69

Figure 4.4 Overview of study area and dataset 70

Figure 4.5 Facies 71

Figure 4.6 Sandstone body width measurements 72

Figure 4.7 Very narrow sandstone bodies 73

Figure 4.8 Narrow sandstone bodies 74

Figure 4.9 Medium sandstone bodies 75

Figure 4.10 Sheet/other sandstone bodies 76

Figure 4.11 Cross-cutting relationships and superposition 77
Figure 4.12 Depositional model 78
Figure 4.13 Interpreted barform 79
Figure 4.14 Schematic for barform evolution 80
Figure 4.15 Sedimentary logs from the barform 81
Figure 4.16 Paleohydraulic measurements 83
Figure 4.17 Modern analog, Bermejo DFS 84
Figure A.1 Study area and SfM-derived models 100
Figure A.2 Absolute accuracy of the UAV-SfM models 101

LIST OF ABBREVIATIONS

DFS.....Distributive fluvial system

DGPS..... Differential Global Positioning System

DSM.....Digital Surface Model

GCP ..... Ground Control Point

GPR.....Ground Penetrating Radar

GPS ..... Global Positioning System

SfM ..... Structure-from-Motion

TLS .....Terrestrial Laser Scanning

UAV .....Unmanned aerial vehicle

CHAPTER 1

INTRODUCTION

Fluvial deposits serve as petroleum reservoirs, groundwater aquifers, and contain important information on ancient paleogeographies (Miall, 1985, 2006; Martinius and Naess, 2005; Bridge, 2006; Ethridge, 2010; Colombera et al., 2012). These units present serious challenges owing to the complex nature of fluvial systems and their deposits (e.g., Miall, 1996). Studies of modern fluvial systems have been instrumental in gaining insights into these deposits (e.g., Bristow, 1987; Best et al., 2003; Bridge, 2006; Rust et al., 2011), but questions remain concerning the preservation of deposits in the rock record and how well modern fluvial deposits serve as analogs for ancient fluvial deposits (Miall, 2006). As a result, outcrop analogues have long been a critical source of information on the architecture and spatial variability of preserved fluvial systems because they themselves are representative of preserved deposits (Miall, 2006).

Outcrops of sedimentary rocks have long served as the principal source of information for studying fluvial deposits. Such exposures are three-dimensional in nature and contain important information across small (millimeters to meter), intermediate (meter to kilometer), and large (kilometer to 10s kms) scales. Over the years, a variety of methods have evolved to extract data from outcrops (e.g., Buckley et al., 2008; Miall, 1985). Large-scale features have been successfully

captured with aerial photos and satellite imagery (e.g., Hartley et al., 2010; Hubbard et al., 2010; Weissmann et al., 2010), whereas small- to intermediate-scale outcrop features have been recorded with terrestrial laser scanning (TLS), differential GPS, and similar technologies (Bellian et al., 2005; Buckley et al., 2008, 2010; Hajek et al., 2010; Hodgetts, 2013; Rarity et al., 2013; Rittersbacher et al., 2013; Pemberton et al., 2016). Intermediate-scale features, however, are often difficult to characterize as these features are below the resolution of satellite imagery and aerial photos, but larger and more complex than what can be easily recorded with field-based methods. Existing options such as TLS can be helpful for studying small- and intermediate-scale components of outcrops, but may not be appropriate for all investigators as these techniques can involve significant capital costs, training, and specialized equipment. What is needed is an easy-to-use and low-cost technique that will assist in the measurement and interpretation of small- to intermediate-scale features in sedimentary rock exposures.

In addition, ancient fluvial deposits can be extremely complicated due to their inherent three-dimensional nature (variable widths and thicknesses, orientation, degree of amalgamation, etc.). The vast majority of the data and depositional models from ancient fluvial strata are derived from vertical successions or photomosaics, which are exposed either in outcrops or from subsurface data like well-logs and cores (Miall, 1985; Ethridge, 2010). While this data is important to better understand ancient fluvial systems, it falls short of describing variations that can exist within larger systems in- and out-of the

outcrop plan (plan-view). This presents a major limitation in recording the spatial variation across ancient fluvial systems.

Plan-view exposures of ancient fluvial deposits are rare, but where present, have been used to provide insights into depositional histories (e.g., Foix et al., 2012; Ielpi and Ghinassi, 2014; Hartley et al., 2015). However, with few exceptions (e.g., Cuevas martínez et al., 2010), the majority of these examples are limited to individual meander bar deposits or fluvial stories and reconstructions focus on paleohydraulic conditions. Significant questions remain as to how preserved sandstone bodies cross-cut and vary in plan-view space over larger areas (e.g., > 1 km^2) and between fluvial stories.

Here we use unmanned aerial vehicles (UAV), Structure-from-Motion photogrammetry (SfM), and field observations to describe and interpret plan-view exposures of fluvial sandstone bodies in the Salt Wash Member of the Morrison Formation in east-central Utah. Mudstones in this region have been eroded, leaving a 3-D framework of ~flat-lying sandstone bodies, which provide a relatively unique setting to examine plan-view aspects of the deposits.

The aim of this research is to develop and test a workflow that integrates UAV and SfM photogrammetry to develop high-resolution two- and three-dimensional (2-D and 3-D) models and augment them with field-based measurements to aid in sedimentary research. Then to utilize these models to better understand the lateral and vertical variability inherent in ancient fluvial deposits. The objectives of this thesis are:

1. Test and apply a UAV-SfM workflow to fluvial sandstone bodies exposed in plan-view.
2. Test the recently proposed Salt Wash Distributive Fluvial Systems model at an intermediate scale.
3. Reconstruct the planview architecture, and assess variability and trends.

This thesis contains 5 chapters and appendices for the two major chapters (chapters 3 and 4). Within Chapter 2 a literature review is conducted where previous work and background information is given about SfM photogrammetry, UAVs, and a geologic background of the Morrison Formation, the Salt Wash Member from the Morrison Formation, and the Salt Wash as a distributive fluvial system (DFS). Chapter 3 introduces a UAV-SfM workflow and tests its applicability to an outcrop exposed in plan-view. Within this chapter the integrity of the UAV-SfM derived models is assessed by comparing results processed with and without ground control points (GCP). The workflow is then demonstrated on a small barform exposed in plan-view from the Salt Wash Member. Chapter 4 applies the UAV-SfM workflow developed in Chapter 3 to capture roughly 10 km^2 of fluvial sandstone bodies from the Salt Wash Member. The UAV-SfM derived models are augmented with field-based measurements and used to describe the lateral and vertical variability in channel styles, geometry, orientations, and paleocurrents. These results and used to compare them with the current depositional model for the Salt Wash Member and assign an appropriate modern

analog. Chapter 5, the final chapter, is a brief conclusion and summation of the findings found within this thesis.

CHAPTER 2

LITERATURE REVIEW

2.1. Structure-from-motion photogrammetry and unmanned aerial vehicles

SfM involves the use of multiple overlapping images and an image-based terrain extraction algorithm to reconstruct the location of individual points in the photographs in 3-D space (Snavely et al., 2008). Traditional photogrammetry uses overlapping images to determine the location of points within a scene, but prior knowledge of both exterior (the camera location in 3-D space) and interior (geometry and optics of the camera) orientation parameters of the camera is required. With SfM, the images themselves are used to solve the exterior and interior orientation parameters of the cameras without the need to specify a network of targets with known 3-D positions (Snavely et al., 2006; Westoby et al., 2012). This process is performed by automatically identifying keypoints in each image, matching them between overlapping images, and then using an iterative bundle adjustment procedure to recover the camera parameters (Snavely et al., 2008). Once camera parameters are recovered, multi-view-stereo algorithms use the images as inputs and produce 3-D models (e.g. point clouds) with accuracy approaching that of terrestrial laser scanners (TLS) (James and Robson, 2012; Westoby et al., 2012).

SfM, has been applied in several earth science disciplines, including geomorphology, structural geology, and coastal processes (e.g., Westoby et al. 2012; James and Robson, 2012; Fonstad et al. 2013; Javernick et al. 2014; Micheletti et al. 2014; Bistacchi et al. 2015), but has yet to be fully applied to the sedimentary geosciences. Similarly, UAVs have become increasingly important tools in many aspects of the geosciences (Niethammer et al. 2012; Mancini et al. 2013; Bemis et al. 2014; Colomina and Molina 2014; Dietrich 2014; Nex and Remondino 2014; Siebert and Teizer 2014; Gonçalves and Henriques 2015; Ryan et al. 2015; Long et al. 2016). Integrating the mobility of UAVs with the 3-D reconstruction capabilities of SfM provides an alternative way to gather outcrop data, particularly in the small- to intermediate-scale range (e.g., James and Robson, 2012)

Numerous studies have examined the accuracy of SfM reconstructions and products in detail (e.g., Favalli et al. 2012; Turner et al. 2014; James and Robson 2014; Wilkinson et al. 2016). Comparing TLS and SfM has yielded a number of advantages and disadvantages for both methods. TLS has been found to be more robust and obtain higher precision than that of SfM, however, the latter has been shown to be an effective substitute. Westoby et al. (2012) found that decimeter-scale accuracy can still be achieved with SfM and other studies have had similar findings (e.g. Favalli et al. 2012; Wilkinson et al. 2016). What SfM lacks in precision it makes up for in being a low-cost, user-friendly, and portable alternative.

Work has also been done on utilizing UAVs to acquire imagery for SfM photogrammetry. A study by Turner et al. (2012) used a UAV with a navigation grade GPS and achieved an absolute spatial accuracy of 65-120 cm. Turner et al. (2014) later demonstrated that using a UAV with a differential GPS (dGPS) achieved an absolute spatial accuracy of 0.11 m, eliminating the need for GCPs. James and Robson (2014) found that systematic errors can exist from models derived from UAVs, known as vertical 'doming', but these can be largely mitigated by incorporating oblique imagery into the image network.

UAVs come in two main types: fixed-wing and multi-rotor (Fig. 3.2). Fixed-wing UAVs typically have a longer flight time (>30 mins) and are ideal for acquiring high-resolution orthophotos over large areas. Multi-rotor UAVs have a shorter flight duration, but have the advantage of vertical take-off and landing, and the ability to acquire oblique and panoramic imagery. Siebert and Teizer (2014), outlined helpful questions to answer when selecting an appropriate UAV system including: What is the size of the area to be studied? At what altitude does the UAV need to operate? What camera system and what camera mount system (e.g., gimbal) are needed? Are other physical obstacles present? And what take-off/landing space is available? In general, multi-rotor UAVs tend to be better suited for multi-faceted and vertical outcrop exposures with limited take-off and landing areas. Fixed-wing UAVs tend to be better suited for large areas where sedimentary units are exposed on near-horizontal planes. Eisenbeiss (2009) provides a detailed review of UAVs and their use as a photogrammetric measurement tool.

2.2. Morrison Formation

The Morrison Formation consists of fluvial sandstones and nonmarine mudstones, with localized lacustrine and eolian deposits (Craig et al., 1955; Mullens and Freeman, 1957; Tyler and Ethridge, 1983; Currie, 1997; Robinson and McCabe, 1997; Turner and Peterson, 2004; Kjemperud et al., 2008; Weissmann et al., 2013). In most locations it is composed of three members: the lowermost Tidwell Member, the Salt Wash Member, and the uppermost Brushy Basin Member. The Morrison Formation was deposited in the western interior of the United States during the Late Jurassic (Turner and Peterson, 2004). Sediment for the unit is thought to have been supplied by the Sevier Highlands to the west and the Mogollon Highlands to south of the region (Turner and Peterson, 2004). The Morrison Formation does not thicken continuously to the west, as is typical of foreland basin deposits, leading some to propose subsidence in the area was not influenced by flexural loading (Heller et al., 1986). However, others have proposed that the Morrison Formation was deposited in the back-bulge depozone of a flexural foreland basin system that resulted from a Late Jurassic phase of the Sevier orogeny (DeCelles and Currie, 1996; Currie, 1997).

2.2.1 Salt Wash Member

The Salt Wash Member of the Morrison Formation is roughly middle Kimmerdgian in age (Turner and Peterson, 2004) and extends across central Utah, west-central Colorado, northeast Arizona, and northwest New Mexico (Craig et al. 1955; Mullens and Freeman, 1957). The regional extent of the unit

indicates it was associated with a fan-shaped fluvial system that prograded roughly north-eastward (Craig et al., 1955; Mullens and Freeman, 1957; Peterson, 1980, 1984; Tyler and Ethridge, 1983; Kjemperud et al., 2008; Weissmann et al., 2013) from a paleotopographical outlet located near the Mogollon-Sevier highlands syntaxis (Craig et al., 1955; Dickinson and Gehrels, 2008; Owen et al., 2015a). Climate during the time of deposition was likely semi-arid and characterized by variable or seasonal precipitation (Demko et al., 2004; Parrish et al., 2004; Turner and Peterson, 2004; Myers et al., 2014).

The deposits are characterized by multi-story and laterally-amalgamated fluvial sandstones and lesser nonmarine mudstones and siltstsones (e.g., Tyler and Ethridge, 1983). Facies within the Salt Wash Member have been studied extensively, but typically contain very fine-grained sandstones to pebble conglomerates with trough and planar cross-stratification, plane beds, and assymetric ripples, which are interpreted as braided and meandering fluvial deposits (e.g. Peterson, 1980, 1984; Tyler and Ethridge, 1983; Robinson and McCabe, 1997; Kjemperud et al., 2008; Weissmann et al., 2013; Owen, et al., 2015b, 2015c). Pebbles of the Salt Wash Member are typically composed of sand intraclasts, quartz grains, and chert clasts (Robinson and McCabe, 1997; Owen et al., 2015c). Isolated to continuous, red-green, mottled mudstones are present in some areas of the deposit and are interpreted as paleosols and floodplain deposits (Demko et al., 2004). Thin to medium sandstone beds within mudstone packages are interpreted as crevasse splay, minor channel, and overbank deposits (Robinson and McCabe, 1998; Kjemperud et al., 2008; Owen

et al., 2015b, 2015c). Terrestrial bioturbation is present throughout the formation, particularly on the upper portions of fluvial sandstone packages and crevasse splay deposits (e.g., Hasiotis, 2004).

2.2.2. Salt Wash DFS model

The Salt Wash Member is arguably the best example of an ancient DFS, or fluvial megafan (Tyler and Ethridge, 1983; Weissmann et al., 2010; Owen et al., 2015c). Such features are increasingly recognized as important components of clastic depositional systems in basins (Hartley et al., 2010; Weissmann et al., 2010, 2013), but sedimentary details from these deposits are scarce. A modern DFS is defined by: 1) channels that radiate from an apex; 2) a decrease in channel size and abundance downstream; 3) an increase in preservation of floodplain deposits relative to channel deposits downstream; 4) a decrease in grain size downstream; and 5) a change from amalgamated channel deposits in proximal areas to smaller fixed channels in distal areas (Horton and Decelles, 2001; Nichols and Fisher, 2007; Hartley et al., 2010; Weissmann et al., 2010).

The nature of the fluvial sandstone bodies, grain size, and facies change across the region from the southwest to the northeast (Craig et al., 1955; Mullens and Freeman, 1957). In the southwest the unit is dominated by thick, laterally extensive amalgamated channel fill with high connectiveity (Robinson and McCabe, 1997; Kjemperud et al., 2008; Owen et al., 2015c). The grian size is dominantly coarse with very little evidence of floodplain deposits. As you move northeast there is a decrease in thickness and channel belt complexes and are separated by packages of floodplian material (Owen et al., 2015c). The farthest

extent of the Salt Wash Member is dominanted by floodplain material with sparse ribbon channels and an absence of channel belt deposits (Owen et al., 2015c). These regional trends have lead to the conclusion that the Salt Wash Member, along with the underlying Tidwell Member, are part of an ancient Distributive Fluvial System (DFS), referred to as the Salt Wash DFS (Craig et al., 1955; Tyler and Ethridge, 1983; Weissmann et al., 2013; Owen et al., 2015c)

CHAPTER 3

USING UNMANNED AERIAL VEHICLES AND STRUCTURE-FROM-MOTION PHOTOGRAMMETRY TO CHARACTERIZE SEDIMENTARY OUTCROPS: AN EXAMPLE FROM THE MORRISON FORMATION, UTAH, USA[1]

[1]Chesley, J. T., Leier, A.L. White, S., Torres, R., 2017. Submitted to *Sedimentary Geology*, 1/24/2017.

3.1 Abstract

Recently developed data collection techniques allow for improved characterization of sedimentary outcrops. Here, we outline a workflow that utilizes unmanned aerial vehicles (UAV) and structure-from-motion (SfM) photogrammetry to produce sub-meter-scale outcrop reconstructions in 3-D. SfM photogrammetry uses multiple overlapping images and an image-based terrain extraction algorithm to reconstruct the location of individual points from the photographs in 3-D space. The results of this technique can be used to construct point-clouds, orthomosaics, and digital surface models (DSMs) that can be imported into GIS and related software for further study. The accuracy of the reconstructed outcrops, with respect to an absolute framework, is improved with geotagged images or independently gathered ground control points, and the internal accuracy of 3-D reconstructions is sufficient for sub-meter scale measurements. We demonstrate this approach with a case study from central Utah, where UAV-SfM data help delineate complex features within Jurassic fluvial sandstones.

3.2 Introduction

Outcrops of sedimentary rocks have long served as the principal source of information for sedimentary and stratigraphic studies. Such exposures are three-dimensional in nature and contain important information across small (millimeters to meter), intermediate (meter to kilometer), and large (kilometer to 10s kms) scales. Over the years, a variety of methods have evolved to extract data from outcrops (e.g., Buckley et al., 2008; Miall, 1985). Large-scale features have been successfully captured with aerial photos and satellite imagery (e.g., Hartley et al., 2010; Hubbard et al., 2010; Weissmann et al., 2010), whereas small- to intermediate-scale outcrop features have been recorded with terrestrial laser scanning (TLS), differential GPS, and similar technologies (Bellian et al., 2005; Buckley et al., 2008, 2010; Hajek et al., 2010; Hodgetts, 2013; Rarity et al., 2013; Rittersbacher et al., 2013; Pemberton et al., 2016). Intermediate-scale features, however, are often difficult to characterize as these features are below the resolution of satellite imagery and aerial photos, but larger and more complex than what can be easily recorded with field-based methods. Existing options such as TLS can be helpful for studying small- and intermediate-scale components of outcrops, but may not be appropriate for all investigators as these techniques can involve significant capital costs, training, and specialized equipment. What is needed is an easy-to-use and low-cost technique that will assist in the measurement and interpretation of small- to intermediate-scale features in sedimentary rock exposures.

Here, we explain how the combination of camera-mounted unmanned aerial vehicles (UAVs) and structure-from-motion (SfM) photogrammetry can be applied to sedimentary outcrop studies. SfM, which uses digital photos to create 3-D reconstructions, has been applied in several earth science disciplines (e.g., James and Robson, 2012; Westoby et al., 2012; Fonstad et al., 2013; Javernick et al., 2014; Micheletti et al., 2014; Bistacchi et al., 2015), but has yet to be fully utilized in sedimentary studies. Similarly, UAVs are becoming increasingly effective tools in the geosciences (Niethammer et al., 2012; Mancini et al., 2013; Bemis et al., 2014; Colomina and Molina, 2014; Dietrich, 2014; Nex and Remondino, 2014; Siebert and Teizer, 2014; Gonçalves and Henriques, 2015; Ryan et al., 2015; Long et al., 2016). Integrating the mobility of UAVs with the 3-D reconstruction capabilities of SfM provides an alternative way to gather outcrop data, particularly in the small- to intermediate-scale range (e.g., James and Robson, 2012). SfM and UAVs will not replace existing data collection techniques, but their use offers a relatively easy and effective way to augment traditional methods. This paper includes a brief overview of SfM and UAVs, as well as a case study demonstrating their applicability to outcrop-based investigations.

3.3 Structure-from-Motion Photogrammetry

SfM involves the use of multiple overlapping images and an image-based terrain extraction algorithm to reconstruct the location of individual points in the overlapping images in 3-D space (Fig. 3.1; Snavely et al., 2008). Traditional photogrammetry uses overlapping images to determine the location of points

within a scene, but prior knowledge of the cameras exterior (location in 3-D space) and interior (geometry and optics) orientation parameters is required. With SfM, the images themselves are used to solve the exterior and interior orientation parameters of the cameras without the need to specify a network of targets with known 3-D positions (Snavely et al., 2006; Westoby et al., 2012). This process is performed by automatically identifying keypoints in each image, matching them between overlapping images, and then using an iterative bundle adjustment procedure to recover the camera parameters (Snavely et al., 2008). Once camera parameters are recovered, multi-view-stereo algorithms use the images as inputs and produce 2- and 3-D models (e.g. orthomosaic and point clouds) with accuracy approaching TLS (James and Robson, 2012; Westoby et al., 2012).

3.4. UAVs and Data Acquisition

3.4.1. Unmanned Aerial Vehicles

The digital photos used in SfM can be acquired from different platforms, including hand-held cameras, balloons, kites, and UAVs. UAVs are particularly effective for collecting digital images of sedimentary outcrops on intermediate-scales (m to km), and in areas that are not easily accessible. UAVs come in two main types: fixed-wing and multi-rotor (Fig. 3.2). Fixed-wing UAVs typically have a longer flight time (>30 mins) and are ideal for acquiring high-resolution orthophotos over large areas. Multi-rotor UAVs have a shorter flight duration, but have the advantage of vertical take-off and landing, and the ability to acquire oblique and panoramic imagery. Siebert and Teizer (2014) outlined helpful

questions to answer when selecting an appropriate UAV system including: What is the size of the area to be studied? At what altitude does the UAV need to operate? What camera system and what camera mount system (e.g., gimbal) are needed? Are other physical obstacles present? And what take-off/landing space is available? In general, multi-rotor UAVs tend to be better suited for multi-faceted and vertical outcrop exposures with limited take-off and landing areas. Fixed-wing UAVs tend to be better suited for large areas where sedimentary units are exposed on near-horizontal planes. Eisenbeiss (2009), provides a detailed review of UAVs and their use as a photogrammetric measurement tool.

3.4.2. Image acquisition strategies

Digital photographs are the basic input for SfM reconstructions; thus, digital cameras are the principal data-gathering tools. As with any photogrammetric technique, the quality of the input images constrains the output quality of the model. Cameras with as little as 5 MP have produced successful results (Micheletti et al., 2014). A digital SLR camera equipped with a fixed focus lens will generate the most accurate data, whereas widely varying zoom settings introduce instability (Shortis et al., 2006). Geotagging the images during acquisition can increase the accuracy and the processing time. Turner et al. (2014) demonstrated that an absolute spatial accuracy of <1 m could be achieved with geotagged images. Cameras without geotagging capabilities can still be used but require constraints from ground control points (GCPs) in the processing stage.

The optimal strategy for acquiring the necessary number of photos and degree of overlap is both location- and objective-specific. In our experience, an overlap of >60% between adjacent photos is typically sufficient. Areas with less contrast (e.g., deserts) may need a higher overlap to produce optimal results. The total number of photos needed is a function of the size of the area and the amount of overlap between images. As a general rule, key features in the reconstruction should be visible in a minimum of three photos in order for the SfM algorithm to locate individual points. Fewer photos can result in gaps, holes, or distortions in the SfM-models. However, an excessive number of photos can result in prolonged processing times and unnecessarily large files that can be difficult to manipulate during post-processing. Overall, it is better to take more photos than fewer, as SfM processing software typically allows for selective use of images.

3.5. Data processing

Once the digital images of the outcrop are acquired, they need to be input into SfM processing software, which can be used to produce exportable, georeferenced point-clouds, triangular meshes, orthomosaics and digital surface models (DSMs). SfM processing software comes in both open-source and commercial packages. Bundler (Snavely et al., 2006) and VSFM (Wu, 2013) are two commonly used, open-source programs that take the input photos and produce 3-D point clouds, which can be further processed with additional software (e.g., PMVS2; Furukawa and Ponce, 2010). Commercial software

packages such as Agisoft Photoscan™, and Pix4Dmapper™ provide the benefit of automated workflows.

Data processing can vary between software packages, but the SfM workflow typically contains the following steps: 1) identification of keypoints in each image; 2) matching of keypoints between images; 3) automatic aerial triangulation (AAT) and bundle block adjustments (BBA) to estimate camera pose; 4) processing of the oriented photos to obtain a point cloud; and 5) DSM and orthomosaic generation (Fig. 3.3). During the initial processing images are uploaded and a matching algorithm (e.g., SIFT) is used to identify correspondences between images (Lowe, 1999, 2004). AAT uses the correspondences to triangulate the 3-D positions of the points; BBA is then used to reconstruct the position and orientation of the camera for every acquired image (Tang et al., 1997; Triggs et al., 2000). Each computed 3-D point, which was initially detected using AAT is associated with a corresponding 2-D keypoint on the images. Keypoints are then verified and their 3-D coordinates are calculated (tie-points), producing a sparse 3-D point cloud. Multi-view stereo algorithms use the tie-points and estimated camera parameters as inputs for SfM models, generating the densified point cloud, DSM, and orthomosaic.

3.6. SfM Accuracy

Numerous studies have examined the accuracy of SfM reconstructions in detail (e.g., (Favalli et al., 2012; James and Robson, 2012, 2014; Westoby et al., 2012; Micheletti et al., 2014; Turner et al., 2014; Wilkinson et al., 2016). For outcrop studies, we are primarily interested in two types of accuracy: *absolute*

and *relative*. Absolute accuracy refers to the difference between the location of a point on Earth (e.g., latitude, longitude, and elevation) and the reconstructed position of the same point in the SfM output. Relative accuracy is a measure of positional consistency between a data point relative to nearby data points; it reflects the similarity of the measured distances between points on Earth, and the corresponding distances in the SfM output. For sedimentary outcrop studies, relative accuracy is arguably more important; a high degree of relative accuracy means that SfM reconstructions can be used to acquire quantitative measurements (e.g., lengths and angles) of outcrop features. Whether these features are accurately located in absolute space is typically less important.

Prior to applying the UAV and SfM technique to outcrops, we tested both the absolute and relative accuracy of our reconstructions on open fields near Columbia, South Carolina, USA (Appendix A). In absolute space, the UAV-SfM technique had an average horizontal and vertical offset of 1-3 m, as measured by comparing SfM reconstructions done with GCPs and without GCPs. The relative accuracy was assessed by comparing measurements of objects in the SfM reconstructions with ground-based measurements of those same features. A one-way variance test between these measurements yielded no statistically significant differences, indicating a very high degree of relative accuracy within the SfM reconstructions. The combination of previous studies and our test results provides confidence that the UAV-SfM technique is suitable for examining outcrop features at intermediate scales (meters – kilometers). Nonetheless, we

recommend that all investigators test accuracies with control measurements before undertaking outcrop studies.

3.7. Case Study

To demonstrate the applicability of the UAV-SfM technique to sedimentary outcrops, we examined exposures of the Salt Wash Member of the Morrison Formation in east-central Utah (Fig. 3.4). The Salt Wash Member is composed of multistory and multilateral fluvial sandstone bodies interbedded with floodplain mudstones and siltstones (e.g., Tyler and Ethridge, 1983). South of Green River, Utah, USA, the less resistant mudstones in the Salt Wash Member have been eroded, leaving a 3-D framework of ~flat-lying sandstone bodies (Jones and Gustason, 2006), which provide a perfect natural laboratory to examine vertical and plan-view exposures of ancient fluvial deposits. Large-scale features in the area are identifiable in satellite imagery (e.g., Google Earth™), and small-scale features (grain-size, sedimentary structures) can be recorded with field-based observations. However, the intermediate-scale features, which include the internal details of sandstone bodies, and those features that help tie the field-based observations to the large-scale exposures, are impossible to document without an additional dataset (Fig. 3.4B). To bridge this data gap and aid in our interpretation, we employed the UAV-SfM technique to capture and map the intermediate-scale features of a portion of this area (Fig. 3.5).

Images were collected using an autonomous, fixed-wing, UAV (eBee™, Sensefly Ltd.) that carried an 18.2 MP digital camera (Sony) with a 25 mm focal length lens (Fig. 3.2B). The UAV is equipped with an on-board artificial

intelligence system that analyzes data from an inertial measurement unit and an on-board GPS to optimize the flight. The flight was planned and operated using eMotion2^{TM} software. Flights were made at an altitude of 92 m (302 feet) above the local ground surface and images were acquired with a lateral and longitudinal overlap of 80%. In total, 516 images were acquired, covering an area of 0.87 km^2, and requiring a flight time of approximately 30 minutes (Fig. 3.5A). Field-based observations and paleocurrent measurements (n = 152) were collected in the field to supplement the models with qualitative and quantitative information. The images were processed using Pix4Dmapper^{TM} (Pix4D) photogrammetry-software, which groups the workflow into three steps: 1) initial processing; 2) point cloud densification and 3-D mesh generation (Fig. 3.5B); and 3) DSM and orthomosaic generation (Fig. 3.5C-D). The densified point-cloud contains 62.8x10^6 points, with an average density of 117.92 points/m^2. The orthomosaic and DSM resulted in a resolution of 2.69 cm/pixel. A series of control measurements made on the ground were identical to the same measurements made in the SfM reconstruction, indicating high relative accuracy. The entire process, including flight time and data processing, took approximately 5 hours. The resulting orthomosaic and DSM were imported into ArcMap (10.3), where individual features were mapped and augmented with field-based observations.

The UAV-SfM produced orthomosaics and DSM provide a high-resolution image of the field area and highlight several features that could not be observed from the ground or with existing aerial imagery (Fig. 3.6). The northern margin of the sandstone body is convex to the north, whereas the southern boundary of the

exposure is a cliff face. The north-south width of the sandstone body varies from 56 m in the west, 115 m in the center, and 65 m in the east. Internally, several distinct architectural elements are identifiable and mappable in the orthomosaic and DSM (Figs. 3.7, 3.8). The majority of the surfaces within the sandstone body are convex-northward, similar in trend to the northern boundary, with the exception of one unit in the west-central area, which trends to the northwest-southeast (Fig. 3.7). A series of west-east and northwest-southeast trending curvilinear sandstone bodies and surfaces are present in the east-central area, which based on their orientation and related paleocurrent data are interpreted as lateral accretion sets (Fig. 3.7). The northernmost periphery of the sandstone body contains a traceable architectural element ~17 m in width and 390 m in length (Figs. 3.7, 3.8).

The resolution and 3-D nature of the orthomosaic, DSM, and point-cloud enable additional quantitative measurements to be made with this dataset. Widths and lengths of individual features are easy to measure with SfM data. Based on our experience, the SfM measurements are more accurate than those made on the outcrop given the uneven terrain and obstacles (e.g., bushes), and can be made in a fraction of the time (Fig. 3.8). The high resolution of the orthomosaic and DSM enable paleocurrent data to be estimated from meso- to macro-scale sedimentary structures (Fig. 3.8), which can augment ground-based measurements and be used to collect data from inaccessible locations. In addition to 2-D measurements, volumes of features and sandstone bodies can be calculated directly from the point cloud; for example, the sandstone exposure

in Figure 3.9 has a volume of 168.77 ±6.09 m^3. In addition, the geolocated point cloud can be imported into more comprehensive modeling software, where it can provide a 3-D framework for more detailed characterization (e.g., Enge et al., 2007).

Based on the overall morphology, sedimentary characteristics, and paleocurrent data, we interpret this sandstone body as the deposit of an internally complex, laterally-accreting barform. The orientation of the accretion sets in the eastern portion of the sandstone suggest both lateral- and down-stream migration with respect to the dominant paleoflow direction (Fig. 3.8). The preserved morphology of the sandstone body is suggestive of a point-bar in a meandering river system, but without the complete exposure (the southern margin is eroded) there is a possibility this sandstone was deposited by a laterally accreting bar in a multichannel system (i.e., braided river). Regardless, the UAV-SfM data capture a complex array of depositional features that would have been difficult if not impossible to determine without this dataset. These details can be critical for understanding analogous reservoirs and aquifers.

Although this particular study focuses on sedimentary strata that are exposed in plan-view, this methodology and workflow is just as applicable to vertical or inclined outcrop exposures. The general procedures used to acquire, process, and interpret data from a vertical outcrop exposure are the same, although a multi-rotor UAV or alternative platform may be more appropriate. The data from a vertical outcrop face would provide the same basis for correlation, measurements, and interpretation as outlined in the case study.

3.8. Conclusion

The combined use of UAVs and SfM photogrammetry provides an effective way to acquire additional data from sedimentary outcrop exposures. This method is particularly useful for intermediate-scale features and helps bridge the gap between existing aerial imagery and ground-based observations. In addition, SfM records the 3-D nature of outcrops, making it perfect for capturing complicated exposures. The use of UAVs in image acquisition allows larger areas to be studied, including exposures that are inaccessible by foot (e.g., vertical cliff faces). Although it should be tested prior to use, the 3-D reconstructions made from UAV-SfM can achieve a relative accuracy to a sub-meter scale and can be used to gather quantitative data from outcrop exposures. That being said, this method is not without limitations. In terms of quality, TLS data yield far higher resolution and show more consistency relative to SfM (Wilkinson et al., 2016). The prices of UAVs are decreasing, however such devices are not without initial costs and many require operator training before use. In addition, UAVs cannot be used everywhere; UAVs are regulated by federal and local agencies, which should be consulted prior to their use. Despite these drawbacks, the combined use of UAVs and SfM photogrammetry represents a promising new tool for characterizing and studying sedimentary outcrops.

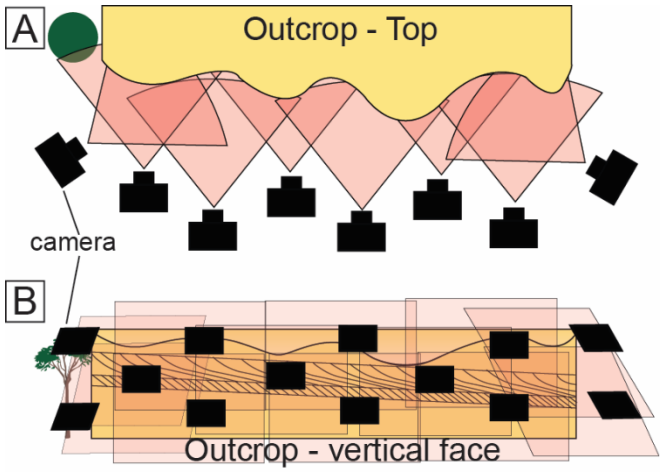

Figure 3.1. Schematic of structure-from-motion (SfM) photogrammetry. SfM photogrammetry uses multiple overlapping images and an image-based terrain extraction algorithm to reconstruct the location of individual points in 3-D space. A) View of an outcrop from above, with cameras. B) Ground-based view of the outcrop, including camera locations.

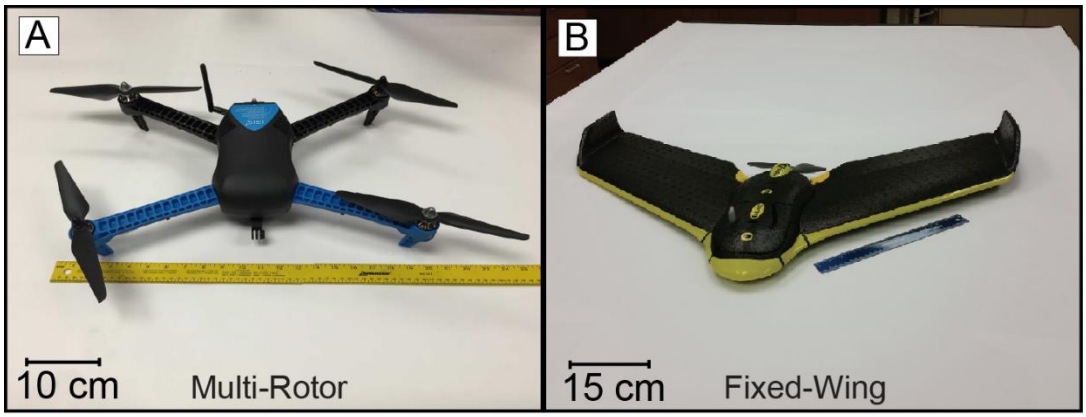

Figure 3.2. Examples of different unmanned aerial vehicles (UAVs). A) Quadcopters have the advantage of high mobility and are well suited for vertical and multifaceted outcrops exposures. B) Fixed-winged UAVs can cover large areas and are typically better suited for outcrop faces that are non-vertical.

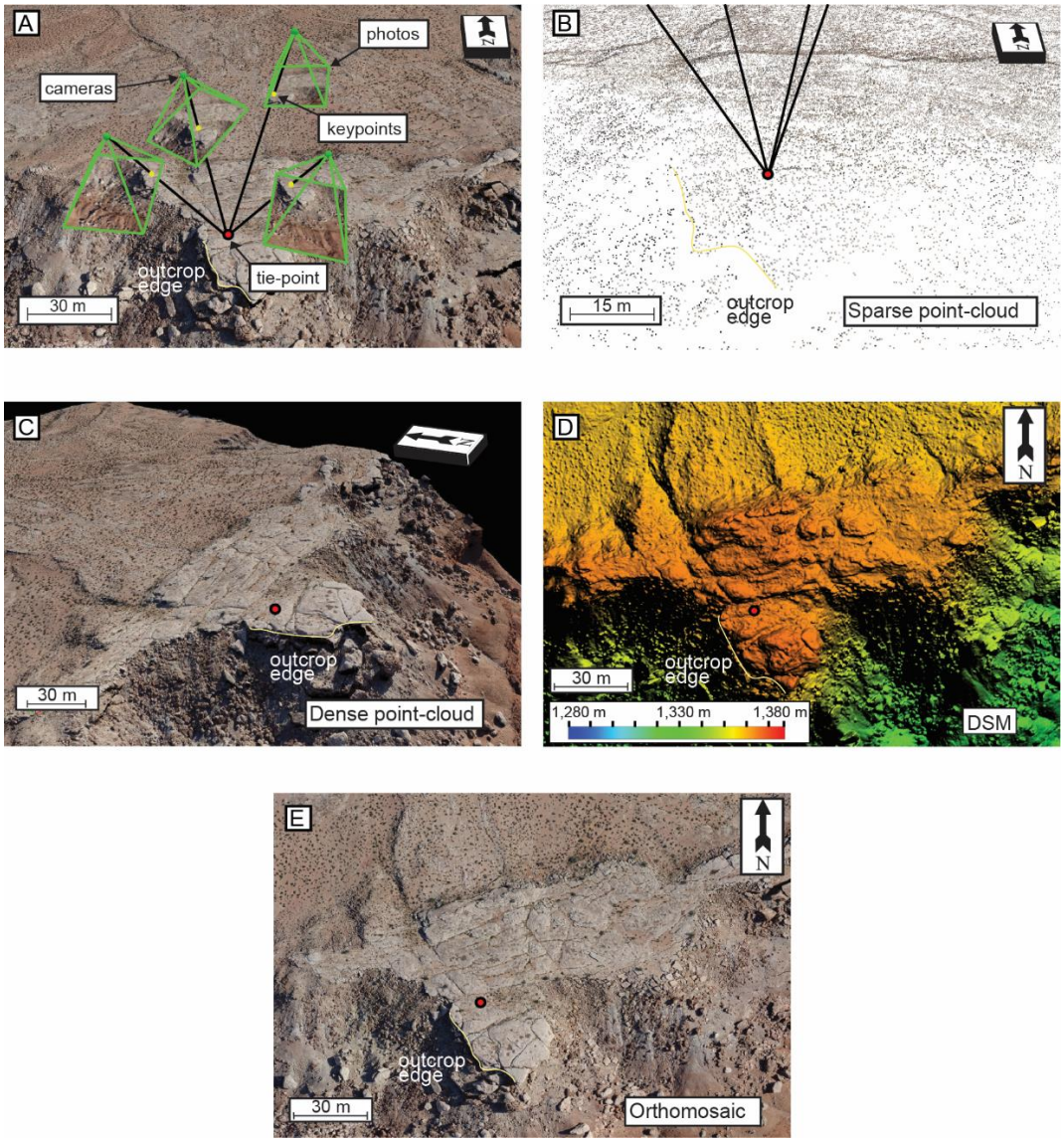

Figure 3.3. A) SfM photogrammetry concept. Green spheres represent camera locations, green squares show the digital images. The outcrop of interest is in the background. Outcrop edge is shown in each image to assist orientation. Multiple overlapping images are taken and a matching algorithm identifies keypoints in each image (yellow dots) and corresponding keypoints are matched between images. B) The location of those keypoints are triangulated and projected into a 3-D space (black ray traces) generating tie-points (red dot), creating a sparse 3-D point-cloud. C) Following this, a densified point-cloud and mesh are generated from the sparse-point cloud. D and E) The densified point-cloud and the calibrated images are used to obtain elevation information and remove perspective distortion to generate the orthomosaic and DSM.

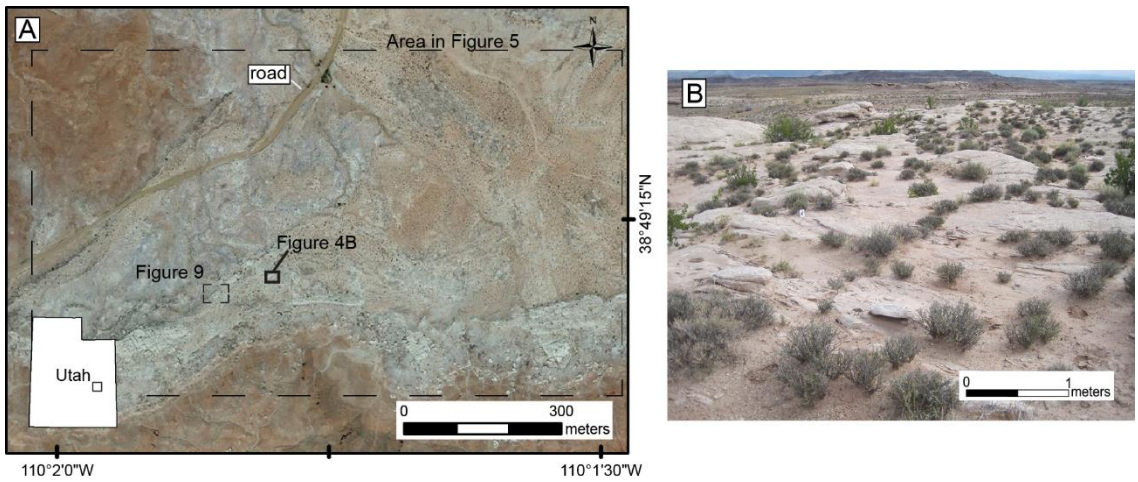

Figure 3.4. Case study area. A) The Salt Wash Member of the Morrison Formation is exposed south of Green River, Utah. Image is from GoogleEarth™, vertical perspective. Mudstone units have been eroded, leaving a framework of relatively flat-lying sandstone bodies exposed at the surface. Although larger-scale features can be seen in these images, details cannot be delineated. B) Photo of the outcrop exposures from ground-view. At this scale, small-scale features can be observed and measured, but larger-scale sandbodies, like that in (A) are not discernable.

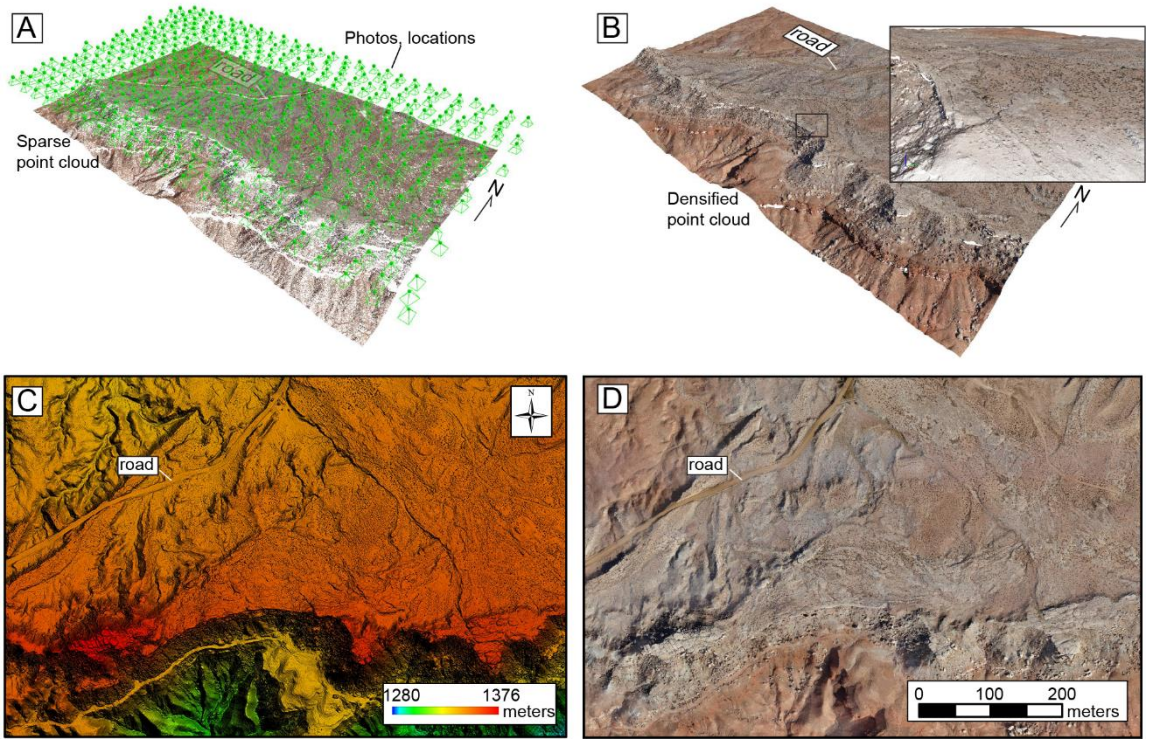

Figure 3.5. Data acquisition from the case-study area. A) An oblique perspective image of the sparse point cloud created from SfM. For location and scale, see Figure 4. Green circles and rectangles above the point cloud represent the locations of the photos collected by the UAV as it flew above the study area. These images were used to create the sparse point cloud. The same road is denoted in each figure to help with orientation. B) Densified point cloud created from the sparse point cloud, same perspective as in (A). Inset shows a smaller scale subset of the densified point cloud, depicted with a black box. C) Vertical perspective of the DSM created from the images and SfM processing. Vertical scale is displayed in meters above sea level. Horizontal scale is the same as in (D). Orthomosaic of the study area, vertical perspective.

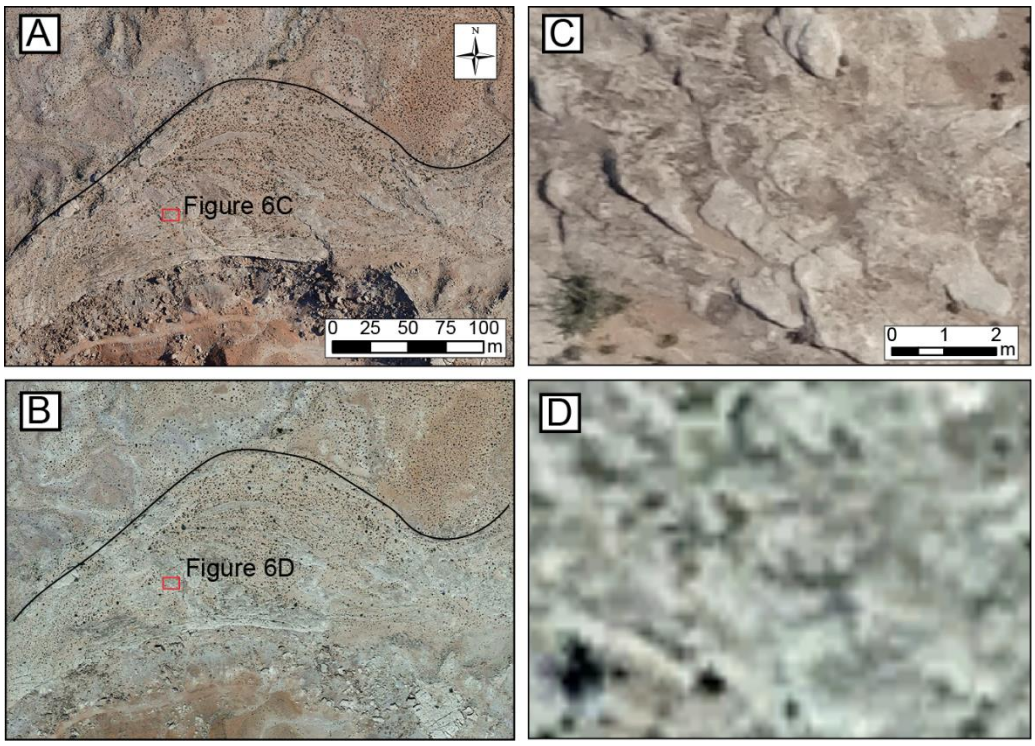

Figure 3.6. Comparison between UAV-SfM data and GoogleEarth™ imagery. A) Regional (vertical) view of the case-study area from UAV acquired images. Black line outlines the northern margin of a sandstone body. B) Same area as in (A) from GoogleEarth™. C) Zoomed-in view of the outcrop from the UAV acquired data. D) Zoom in view of the same area in (C) from GoogleEarth™. Several datasets can be used to capture larger-scale features in the outcrop; however, intermediate- to small-scale features are below the resolution of most available satellite imagery and aerial photos.

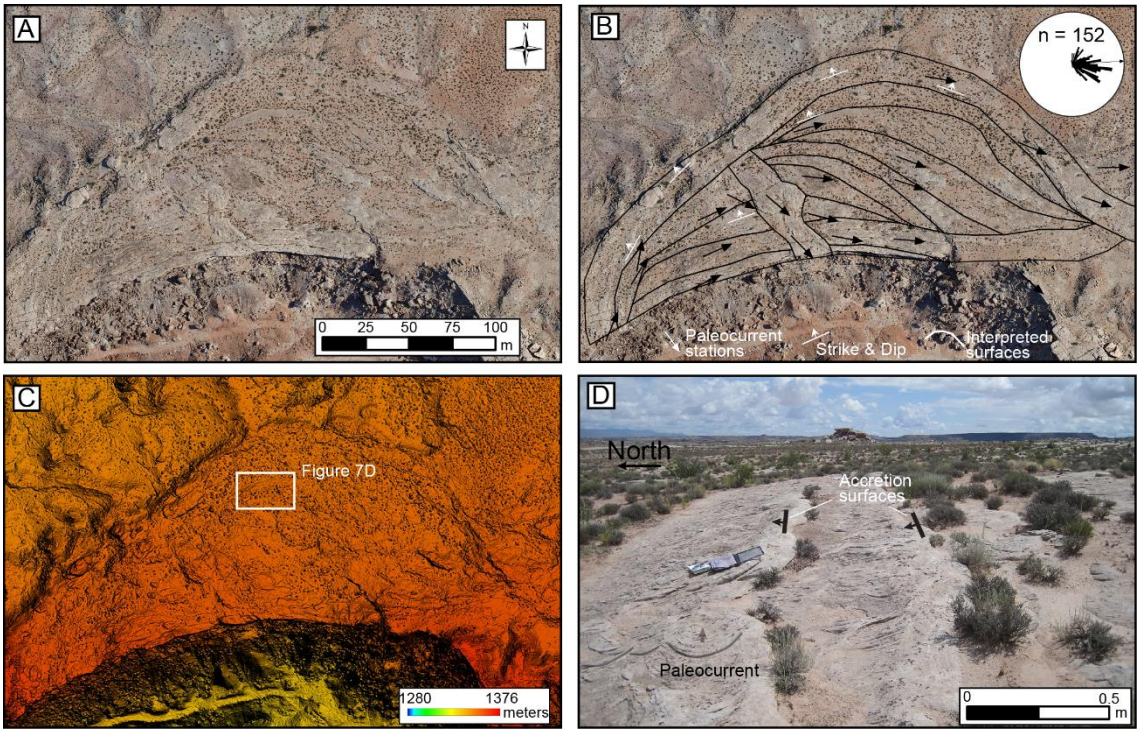

Figure 3.7. Sandstone body and geologic interpretations from the case study. A) Orthomosaic of the sandstone body exposed in the study area. B) Data from the sandstone body, derived from both UAV-SfM imagery and ground-based observations. Individual elements within the sandstone body were mapped using UAV-SfM data and ground based observations. These interpretations were combined with paleocurrent data taken at multiple stations. Arrows show the average for each station. Orientations of surfaces and sandstones are also shown. C) DSM of the same area. In the white box are a series of north-dipping surfaces interpreted as from a laterally accreting barform. D) Ground-based view of the white box in (C), looking towards the east. Paleocurrents record easterly flow, while the accretion sets dip to the north. These features are subtle at ground level, but could be easily identified using ground-based observations and the UAV-SfM data.

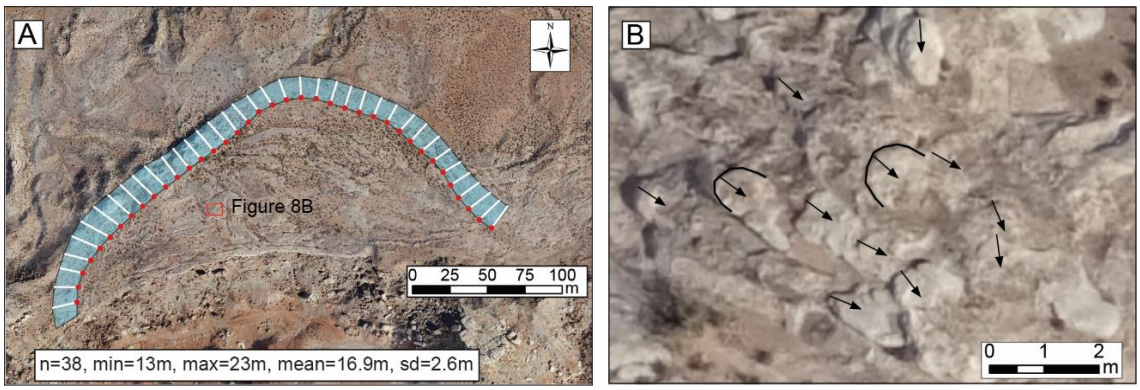

Figure 3.8. Measurements at different scales. A) Larger-scale features, like this linear sandbody element, can be easily measured in GIS software. B) Intermediate- to small-scale features can also be measured from the orthomosaics. Meso-scale sedimentary structures, like these planar-view sets of trough cross-strata, can be measured from the orthomosaic. These features were checked with ground-based observations. The UAV-SfM method provides the ability to acquire additional data from inaccessible portions of outcrops.

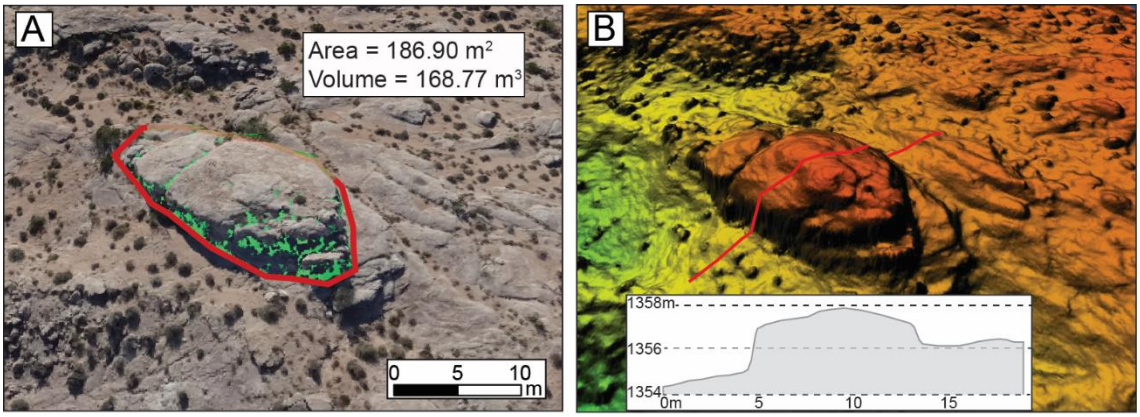

Figure 3.9. Volumetric and area calculations. A) The 3-D nature of the point cloud produced from the UAV-SfM method allows for areas and volumes of outcrops to be easily measured. Here a sandstone is used to demonstrate these capabilities. The red line delineates the measured area. The green represents areas inferred areas lacking keypoints. B) DSM of the same sandstone in (A). Additional measurements can be made from the DSM and 3-D point cloud including vertical distances. The inset shows the topographic profile across the sandstone, depicted by the red line. Vertical scale is in meters above sea-level, horizontal scale is in meters. Location of image is shown in Figure 4.

CHAPTER 4

PLANVIEW VARIABILITY OF FLUVIAL DEPOSITS IN THE SALT WASH MEMBER OF THE MORRISON FORMATION, EAST-CENTRAL UTAH[1]

[1]Chesley, J. T., Leier, A.L., 2017. To be submitted to *Sedimentary Geology*, 1/24/2017.

4.1 Abstract:

Modern fluvial systems are highly variable, often containing the entire spectrum of fluvial styles (e.g., braided to meandering). This variability is difficult to capture in ancient fluvial deposits due to limited 1- and 2-dimesional exposures, which provide only a snapshot of the depositional history at one location. As a result, researchers are forced to interpolate between exposures and develop regional scale models that often underestimate the complexity and variability seen in modern environments. Outcrops of the Upper Jurassic Salt Wash Member of the Morrison Formation in east-central Utah, USA provide an opportunity to examine ancient fluvial sandstone bodies in planview. Here, we characterize the planview architecture of the Salt Wash Member across a 10 km^2 area using unmanned aerial vehicles, structure-from-motion photogrammetry, and field-based observations to gain insight into the lateral and vertical variability in these preserved systems. Overall, sandstone bodies are oriented to the northeast-southwest, with northeasterly paleocurrents, and have widths between 2.5 and 130 m (average 39 m). However, within this spectrum are four distinct types of fluvial deposits, each with its own characteristics. Very narrow sandstone bodies (4-6 m wide) occur in groups, are less than 2 m thick and heavily bioturbated. Narrow sandstone bodies (15 to 45 m wide) are straight to sinuous, contain evidence of lateral migration, and were deposited by east-northeast flowing fluvial systems. Medium sandstone bodies (75 to 105 m wide) are straight, and were deposited by non-migrating, east-flowing fluvial systems. Sheet/other sandstone bodies consist of both sheet-like sandstones whose

edges are not visible and eroded sandstones bodies that cannot be reconstructed. Vertically, these deposits show a stratigraphic pattern that alternates between intervals dominated by narrow and medium sandstone bodies, indicating a cyclical deposition. The succession is consistent with the distributive fluvial system model proposed for the Salt Wash Member. However, the range of sandstone bodies and orientations in this area suggest the DFS deposits may be more variable at local scales (e.g. 10km^2) than what would be predicted by existing large-scale DFS models.

4.2 Introduction

Fluvial strata serve as petroleum reservoirs, groundwater aquifers, and contain important information on continental paleogeographies (e.g., Miall, 1996; Bridge, 2006) However, these deposits can be difficult to predict due to their complicated arrangement in three-dimensional space. Almost all data from ancient fluvial strata are derived from vertical successions, which are exposed in either outcrops or from subsurface data such as well-logs (Miall, 1985; Ethridge, 2010). Whereas these data are crucial and have yielded important descriptive and predictive stratigraphic models, the variability of ancient fluvial deposits in planview space has received far less attention, undoubtedly do to the rarity of such exposures. Seismic data and regional correlations provide information on the larger-scale planview characteristics of fluvial deposits (e.g., Weber, 1992; Hardage et al., 1994; Carter, 2003; Martinez et al., 2004), but details at the barform scale are often below the resolution of these methods. At the other end of the spectrum, planview outcrops of fluvial strata are typically localized and limited to a particular barform or stratigraphic horizon, and have traditionally been used to reconstruct paleohydraulic conditions (e.g., Gawthorpe et al., 1993; Bridge et al., 1995; Foix et al., 2012; Ielpi and Ghinassi, 2014; Hartley et al., 2015). As a result, there are little data on planview architecture of ancient fluvial sandstone bodies over ~1-10 km^2 scales. Questions remain as to whether the planview architecture of fluvial deposits at these scales are consistent with those of regional trends and whether sandstone variability at this scale is predictable.

Here we use unmanned aerial vehicles (UAVs), structure-from-motion photogrammetry (SfM), and field observations to describe and interpret planview exposures of fluvial sandstone bodies in the Salt Wash Member of the Morrison Formation in east-central Utah, USA. Mudstones in this region have been eroded, leaving a 3-D framework of flat-lying sandstone bodies that provide a rare opportunity to characterize planview aspects of the deposits. Based on our measurements, the Salt Wash Member contains a wide array of sandstone bodies, with differing widths, orientations, and shapes. Despite the variability, there are recognizable patterns and trends in the sandstone bodies. Sandstone bodies tend to fall into three width groupings, 4-6 m, 15-45 m, and 75-105 m. These groupings of sandstone body widths tend to have particular characteristics, including orientations and shapes. Stratigraphic horizons in the succession tend to be dominated by sandstone bodies with one particular fluvial style and width. Although collected over a limited area, these data suggest fluvial sandstone bodies in planview contain recognizable patterns, which can be used to better assess reservoir and aquifer models. The overall nature of the sandstone deposits are consistent with previously proposed distributive fluvial system models (DFS). However, existing DFS models focusing on regional trends fail to predict the variability observed over more local (~10 km^2) scales.

4.3. Background

The Upper Jurassic Morrison Formation consists of fluvial sandstones and nonmarine mudstones, with localized lacustrine and eolian deposits that are exposed across a large portion of the western United Sates (Craig et al., 1955;

Mullens and Freeman, 1957; Tyler and Ethridge, 1983; Currie, 1997; Robinson and McCabe, 1997; Turner and Peterson, 2004; Kjemperud et al., 2008; Weissmann et al., 2013). Stratigraphy varies, but in most locations it is composed of three members: the lowermost Tidwell Member, the Salt Wash Member, and the uppermost Brushy Basin Member (Fig. 4.1A). Sediments of the Morrison Formation were derived from the nascent Sevier fold-thrust belt to the west and the Mogollon Highlands to southwest (Turner and Peterson, 2004). The Morrison Formation does not thicken continuously to the Sevier fold-thrust belt, as is typical of foreland basin deposits, which has led some to propose the area was influenced by mantle/dynamic processes (Heller et al., 1986). In contrast, others have proposed that the Morrison Formation was deposited in the back-bulge depozone of a flexural foreland basin system, which resulted from a Late Jurassic phase of the Sevier orogeny (DeCelles and Currie, 1996; Currie, 1997).

The Salt Wash Member of the Morrison Formation is roughly middle Kimmerdgian in age (Turner and Peterson, 2004) and extends across central Utah, west-central Colorado, northeast Arizona, and northwest New Mexico (Craig et al. 1955; Mullens and Freeman, 1957). The regional distribution of the deposits indicate the Salt Wash Member was associated with a fan-shaped fluvial system that prograded towards the northeast from a paleotopographical outlet located near the Mogollon-Sevier highlands syntaxis (Fig. 4.1B) (Craig et al., 1955; Mullens and Freeman, 1957; Peterson, 1980, 1984; Tyler and Ethridge, 1983; Dickinson and Gehrels, 2008; Kjemperud et al., 2008; Weissmann et al., 2013; Owen et al., 2015a). Climate during the time of deposition was likely semi-

arid and characterized by variable or seasonal precipitation (Demko et al., 2004; Parrish et al., 2004; Turner and Peterson, 2004; Myers et al., 2014).

Facies within the Salt Wash Member have been studied extensively and typically consist of very fine-grained sandstones to pebble conglomerates with trough and planar cross-stratification, plane beds, and assymetric ripples, which are interpreted as braided and meandering fluvial deposits (e.g. Peterson, 1980, 1984; Tyler and Ethridge, 1983; Robinson and McCabe, 1997; Kjemperud et al., 2008; Weissmann et al., 2013; Owen, et al., 2015b, 2015c). Pebbles of the Salt Wash Member are typically composed of sand intraclasts, quartz grains, and chert clasts (Robinson and McCabe, 1997; Owen et al., 2015c). Isolated to continuous, red-green, mottled mudstones are present in some areas and are interpreted as paleosols and floodplain deposits (Demko et al., 2004). Thin- to medium-bedded sandstone beds within mudstone packages are interpreted as crevasse splay, minor channel, and overbank deposits (Robinson and McCabe, 1998; Kjemperud et al., 2008; Owen et al., 2015b, 2015c). Terrestrial bioturbation is present throughout the formation, particularly on the upper portions of fluvial sandstones and crevasse splay deposits (e.g., Hasiotis, 2004).

Sandstone body geometries, grain size, and facies change across the region from the southwest to the northeast (Craig et al., 1955; Mullens and Freeman, 1957). In the southwest the unit is dominated by thick, laterally extensive amalgamated channel deposits with relatively coarse-grained sandstone and pebble conglomerate (Robinson and McCabe, 1997; Kjemperud et al., 2008; Owen et al., 2015c). Sandstone units thin to the northeast, and are

interstratified with progressively thicker successions of floodplain mudstones (Owen et al., 2015c). The farthest extent of the Salt Wash Member is dominanted by floodplain material with sparse ribbon channels (Owen et al., 2015c). These regional trends have lead to the conclusion that the Salt Wash Member, along with the underlying Tidwell Member, are part of an ancient DFS, referred to as the Salt Wash DFS (Craig et al., 1955; Tyler and Ethridge, 1983; Weissmann et al., 2013; Owen et al., 2015c).

4.4. Study Area and Methods

4.4.1. Overview

The study area is located 22 km south-southeast of the town of Green River, Utah (Fig. 4.2A), where deposits of the Salt Wash Member are exposed along a west-east trending belt of outcrops that dip gently (<5 degrees) to the north (e.g., Jones and Gustason, 2006). Due to their less resistant nature, the interfluvial mudstones and siltstones have been eroded, leaving a 3-D framework of more resistant sandstone bodies in a planview exposure. In addition, local ledges and canyons provide abundant exposures of the vertical and lateral stratigraphic architecture (Fig. 4.2B). To capture these features, we combined field-based observations, a camera-mounted unmanned aerial vehicle (UAV), and structure-from-motion (SfM) photogrammetry.

4.4.2 Field Mapping

Ground-based field mapping and observations were made in the study area over the course of multiple weeks and included measured sections, photomosaics, and planview mapping of sandstone bodies and architectural

elements. Data collected include thicknesses of sandstone bodies, sedimentary facies characteristics, grain-size trends, depositional surfaces and sandstone architecture, and paleocurrent measurements. Field measurements were recorded using a hand-held. Paleocurrents were collected from individual stations on planview exposures, where at least 7-10 measurements were collected within a 10 m radius. The measurements were collected with a Brunton compass and made from trough-cross strata exposed as rib and furrow structures. Measured sections were recorded at multiple localities where vertical faces were exposed. Photomosaics of vertical exposures were collected, particularly along the southern margin of the study area. All interpretations made from orthomosaics and DSM data were checked in the field wherever possible.

4.4.3 UAV and Image Acquisition

Aerial images of the outcrop exposures were collected with a fully autonomous UAV (eBee, from Sensefly) that carries an 18.2 MP (Sony Cyber-Shot WX) camera with a 25 mm focal length lens. The UAV is equipped with an Inertial Measurement Unit and an on-board GPS. Images were acquired and geotagged automatically by the UAV according to predefined specifications. Flight plans were created prior to going out in the field using eMotion2 software. The UAV flew at an altitude of 105 m (above local surface) and collected images with 80% lateral and longitudinal overlap, yielding a resolution of 3.4 cm/pixel. In order to ensure a consistent quality in all of the images the UAV was flown within the same time interval and similar weather conditions on each flight. A total of 17 flights were flown to cover 12.89 km^2. Flight times varied between flights, but

typically ranged from 30-40 mins. A total of 5,164 images were taken and used for processing. Resolution and accuracy of these data are discussed in Chapter 3.

4.4.4 SfM and Analysis

Images collected during the UAV flights were processed using SfM concepts with Pix4D software. SfM is a photogrammetric technique that utilizes the same principles as stereoscopic photogrammetry, namely that 3-D structure can be resolved from a series of overlapping, offset images (Fig. 4.3; See Chapter 3 for full details). Pix4D uses digital images to generate SfM-derived models including point-clouds (sparse and dense), 3-D meshes, orthomosaics, and digital surface models (DSM). The processing workflow consists of: 1) an initial processing stage, where key points are identified in the images, corresponding points are matched between images, and a sparse point cloud is generated; 2) a secondary stage, where a dense point cloud is generated and colored, and a 3-D mesh is constructed based on the densified point cloud; and 3) a final stage, where the point cloud and images are used to generate a high-resolution orthomosaic and DSM. Due to limited processing power and the sheer size of the dataset (5000+ images) the project was split into 11 subprojects containing a maximum of 500 images and processed separately. Processing time for each subproject averaged around 6.5 hours. All subprojects were georeferenced from the geotagged images using the WGS 1984 UTM Zone 12N coordinate system.

Data were imported into ArcMap where each subproject was properly aligned using a zero-order polynomial shift. Geodatabases were created in ArcMap to store and plot the data collected from the field onto the DSM and orthomosaic images derived from the UAV and SfM photogrammetry. Individual measurements and observation stations were transferred into ArcMap using GPS coordinates collected during field work. The orthomosaic was used to digitally map the exhumed sandstone bodies, which were annotated with observations taken from the field (e.g. paleocurrents, facies etc.). Quantitative information, such as width and area, was extracted from the orthomosaic and DSM datasets. The point-cloud, mesh, and field based observations aided in determining relative stratigraphic relationships between cross-cutting and adjacent sandstones.

4.5. Results and Discussion

4.5.1. General Observations

Sandstone bodies of the Salt Wash Member in the study area include a wide variety of shapes, thicknesses, widths, and orientations. Many of the sandstone bodies in the area are relatively straight with uniform widths along their lengths; however, several sandstone bodies have highly curved outer margins and widths that vary significantly along the length of the exposure (Fig. 4.4). Several smaller sandstone bodies (widths <8 m) are exposed in parallel trending linear groups. Width measurements (n=840) were extracted from 21 distinct sandstone bodies, with 40 measurements made per sandstone body (Fig. 4.4B). These measurements yielded an average width of 39 m, with values between 3 and 130 m. Measured widths are impacted by erosion of the

sandstone bodies, and therefore are probably minimum estimates of original dimensions. The average thickness of sandstone bodies is 4.5 m, but varies between 0.65 and 12 m. Width-to-thickness ratios of sandstone bodies in the study area average of 8.7 (n = 9). The average orientation of the exposed sandstone bodies is 39°; however, the orientations vary nearly 180° and individual sandstone body's cross-cut one another at nearly all angles. Paleocurrent measurements (n=866) indicate a northeast-directed flow, with an average value of 74°, which is generally consistent with previous measurements from the Salt Wash Member in this area (e.g., Owen et al., 2015). Similar to sandstone body orientations, paleocurrents vary over a 180° degree range, from 354° and 173°. Of the entire area, 29% contains visible sandstone bodies, which represents a minimum value considering those that are unobservable or those that have been eroded.

The focus of this study is the planview architecture of the Salt Wash Member, and not specific facies; however, here we provide a brief overview of the lithofacies observed in the field (Fig. 4.5). The Salt Wash Member in this area consists of single- and multistory, ribbon and multilateral fluvial sandstone packages separated by laterally continuous, red and green floodplain mudstones. Sandstones vary from very fine-grained to pebbly, with medium- to coarse-grained sandstones being most common. Trough- and planar-cross strata are present in almost all sandstone successions, along with plane parallel (horizontal) laminations, and asymmetric ripple cross laminations. Uppermost portions of sandstone successions are commonly bioturbated. Granules,

pebbles, and mud rip ups are common in sandstones, particularly near erosive surfaces. Clast-supported pebble conglomerates occur as lenses within sandstones and continuous sheets. Mudstone successions are red and green, mottled, and contain calcium carbonate nodules, root traces and bioturbation. More extensive descriptions of the facies can be found in the following: Tyler and Ethridge (1983); Currie (1997); Kjemperud et al. (2008); Owen et al. (2015b; 2015c).

4.5.2. Sandstone Body Styles and Characteristics

Average widths, thicknesses, orientations, and other measurements obscure several salient trends in the sandstone bodies. Field-based observations and measurements from orthomosaics indicate there are 4 distinct sandstone bodies that can be distinguished based on their widths and additional criteria (Figs. 4.4 and 4.6). In order to be consistent with absolute measuring schemes, we classify these sandstone bodies using Gibling (2006) values, and divide the sandstone bodies into three primary classes: Very narrow sandstone bodies (widths 3-6 m); Narrow sandstone bodies (widths 15-45 m); and Medium sandstone bodies (widths 75-105 m). In addition, we have a class for all other sandstone bodies in the area, termed Sheet/Other, which include sandstone bodies whose edges are obviously eroded or not exposed at the surface (Fig. 4.6).

4.5.2.1. Very Narrow Sandstone Bodies

Very narrow sandstone bodies in the Salt Wash Member have widths of approximately 3-6 m (average = 5 m), are underlain and overlain by mudstone

paleosols, and constitute <1% of the total area. These sandstone bodies are generally exposed in groups with multiple linear bodies of similar dimension oriented parallel to sub-parallel with one another (Fig. 4.7). In cross-section, these units have symmetric lensoid shapes and are typically less than 2 m thick, yielding an average width to thickness (W/T) ratio of 6. Sandstones are very fine- to fine-grained and moderate to well-sorted. These units are commonly heavily bioturbated, including root traces and unidentified terrestrial burrows (Hasiotis, 2004). Where present, sedimentary structures include trough-cross strata, horizontal lamination, and current ripples. In planview, the very narrow sandstone bodies are typically straight to slightly sinuous with relatively constant widths along their lengths. These are present throughout the study area but are best exposed adjacent to larger sandstone bodies, although not necessarily at the same stratigraphic horizon. While these features show a mean orientation to the northeast (avg. = 31°), they display the widest variation of all the sandstone bodies.

The very narrow sandstone bodies are interpreted as deposits of small (<8 m width) channels that occupied floodplain environments of the Salt Wash fluvial system. Extensive bioturbation within these units suggests that once deposited, the sediment was exposed to plant, insect, and animal activity. These are interpreted as crevasse channel and splay deposits, some of which may have been influenced by animal trackways (Jones and Gustason, 2006).

4.5.2.2 Narrow Sandstone Bodies

Narrow sandstone bodies are present throughout the study area (Fig. 4.8), constituting 2% of the total area. Narrow sandstones range in width between 15-45 m, with an average width of 26 m. Widths are typically consistent along the length of the sandstone bodies; however, widths can vary considerably along the length of particular examples, particularly where outer margins are arcuate and the body itself widens and narrows along its length. Thicknesses of sandstone bodies are variable, but generally between 2 and 4 m, yielding an average W/T of 9. These sandstone bodies typically have both symmetric and asymmetric cross-sections. Individually, the sandstone bodies represent single story deposits and are typically straight to slightly sinuous (sinuosity ~1.1) over their exposed lengths. The majority of the examples do not contain evidence of lateral migration, although there are several exceptions. In the southern portion of the study area, one example displays clear evidence of a laterally migrating barform and has a sinuosity value of 1.3 (see below; Fig. 4.13). Surface separating architectural elements within individual sandstone bodies are common and present in both planview and vertical exposures. Internally, these features are composed of medium- to coarse-grained sandstone with trough-cross strata, and lesser planar cross-strata, plane-parallel laminations and rare current ripple cross-laminations. Rare lenses of clast-supported granule- to pebble-conglomerate occur within these sandstone bodies throughout the study area. The uppermost portion of individual sandstone bodies is commonly bioturbated. These features are preferentially oriented toward the north-northeast, avg= 28°,

with a range between 340° and 120°. Paleocurrents indicate flow directions to the north-northeast (average = 65°, n=313).

The narrow sandstone bodies are interpreted to have been deposited by straight to sinuous fluvial channels that transported sand- to pebble-size sediment to the north-northeast. The majority of these sandstone bodies do not have evidence of lateral migration, suggesting straight to sinuous, fixed-channels. However, several examples in the study area contain clear evidence of lateral migration and are consistent with meandering river facies models (e.g., Miall, 1996).

4.5.2.3. Medium Sandstone Bodies

Medium sandstone bodies represent 7% of the total area and have widths typically between 75-105 m and an average width of 85 m (Fig. 4.9E). Widths are consistent along the length of these sandstone bodies. Individual sandstone bodies have thicknesses between ~4-8 meters, yielding an average W/T ratio of 11. These are both single and multistory, and typically straight (sinuosity ~1); individual stories tend to have symmetric cross-sectional forms. The medium sandstone bodies contain little to no evidence of lateral migration (Fig. 4.9A-D). Surfaces separating architectural elements within individual sandstone bodies are common and present in both planview and vertical exposures. Medium sandstone bodies are composed of fine- to coarse-grained sandstone with discontinuous lenses of clast-supported granule- and pebble-conglomerate. Trough cross-strata, planar cross-strata, plane parallel beds and laminations, and rare current ripple cross-laminations are present throughout the sandstone

bodies. Macroform features include sets of low-angle, inclined beds dipping in both the same direction and orthogonal to paleocurrent directions. Uppermost surfaces of individual sandstone bodies are commonly bioturbated. These sandstone bodies are oriented to the east and east-southeast (avg=87°, n=7). Paleocurrents (n=135) correspond to the overall orientation of the sandstone body and average 89°, with a range between 10° and 155°(Fig. 4.9F).

The medium sandstone bodies are interpreted as deposits of larger (relative to the narrow and very narrow sandstone bodies), non-migrating channels that contained downstream and laterally accreting bars. While the calculated sinuosity signifies a system of straight channels there are several that display gentle curvature (Fig.4.6). These sandstone bodies are similar to others documented in the Salt Wash Member, which are attributed to relatively straight, fixed-channel fluvial systems(e.g., Owen et al., 2015c).

4.5.2.4. Sheet/Other Sandstone Bodies

Sheet/Other sandstone bodies are scattered across the study area and represent 19% of the total area. These sandstone bodies represent two primary types of exposures: 1) Sandstone bodies that are highly eroded, such that original dimensions cannot be determined; 2) “Sheet” sandstone bodies that are relatively wide (>100 m), and whose margins are not exposed, precluding measurements. Those sandstone bodies that are highly eroded are generally associated with the uppermost portion of the Salt Wash Member, and have been eroded to such an extent that no planview information can be gathered. The sheet sandstone bodies are 5-12 m thick and composed of medium- to coarse-

grained sandstone with interbedded granules. Along the southern edge of the study area at least three of these successions are visible, each separated by packages of floodplain material (Fig.4.10). Paleocurrents are toward the east with an average paleoflow direction of 73° (n = 283). Vertical exposures reveal multilateral channel belt packages. Internally, the sandstone bodies contain both lateral and downstream accreting surfaces.

The sheet sandstones are interpreted as laterally continuous sandstone bodies deposited by braided river systems or through the lateral amalgamation of individual channel deposits in a relatively low accommodation/sediment supply system. Both braided river systems and amalgamated fluvial channels can produce wide, laterally continuous sandstone bodies (Miall, 1996; Owen et al., 2015c). The similarity between the paleocurrent directions of the medium sandstone bodies and the sheet sandstone bodies supports the hypothesis that these sheet sandstones may represent amalgamated channel deposits, however the braided river hypothesis cannot be excluded.

4.5.2.5 Discussion

Sandstone bodies of the Salt Wash Member exposed across the study area are highly variable, with a broad range of thicknesses, widths, shapes, and orientations. Whereas the average values from all of these deposits are consistent with general trends and previous studies (e.g., Tyler and Ethridge, 1983; Currie, 1997; Robinson and McCabe, 1997; Kjemperud et al., 2008; Owen et al., 2015a, 2015b, 2015c), these average values hide recognizable patterns within the data set. Our data suggest at least 4 types of sandstone bodies are

present in the area, each with their own characteristics. Very narrow sandstone bodies are 4-6m wide, straight, and heavily bioturbated features that are typically present in groups. Narrow sandstone bodies are 15-45 m, straight to sinuous, and north-northeast oriented features. Medium sandstone bodies are 75-105 m wide, straight, and east-southeast oriented features. Sheet sandstone bodies are wide >100 m features with paleocurrents directed to the east.

These findings have several implications for reconstructing ancient fluvial deposits and for predicting subsurface equivalents. Sandstone bodies in this portion of the Salt Wash Member record deposition by different fluvial systems, each with their own particular characteristics. Evidence of both laterally migrating and fixed-channel systems are present in the area, along with a relatively wide range in the size of the original fluvial channels. The medium sandstone bodies, for example, are not simply the product of amalgamated narrow sandstone bodies, but were deposited by relatively larger fluvial channels that were oriented >45° from the ancient rivers that deposited the narrow sandstone bodies. As a result, the distribution of sandstone body properties is not normally distributed about the average of the entire group. This is most evident in the width measurements, where there are three populations within the overall measurements. Distributions like these may be an important constraint for numerical models of flow in reservoirs and aquifers, which typically require a programed range and distribution of values.

4.5.3. Vertical trends in sandstone body characteristics

4.5.3.1 Description

The Salt Wash Member in this area contains a distinct vertical stacking pattern, which most evident when the succession is divided into several stratigraphic intervals. The lack of distinct through-going surfaces or beds within the study area preclude a definitive subdivision of the strata; however, field based mapping and high-resolution DSM data allow us to divide the succession into approximate intervals based on superposition and cross-cutting relationships (Fig. 4.11). Based on similarities in specific stratigraphic horizons, we break up the succession into 4 layers or intervals, which we assume approximate relative periods of deposition. Obviously, it is unlikely that all sandstone bodies within a single interval were deposited simultaneously, or that the channels responsible for their deposition were active at the same time. However, we assume the sandstone bodies in these intervals were deposited prior to sandstone bodies in overlying intervals.

Interval 1, represents the lowermost interval of sandstone bodies visible in planview in the study area (Fig. 4.12A). In some locations this interval represents the lowermost sandstones of the Salt Wash Member exposed in planview, in other areas there are relatively thin (~1.5 m) laterally discontinuous sandstone bodies beneath this interval. Interval 1 overlies a prominent red paleosol that can be traced across much of the study area. The sandstone bodies in this interval are characterized by their narrow widths (26 m), and north-northeast trends (Fig. 4.8). Several of the sandstone bodies are either sinuous and/or contain evidence

of lateral migration. These sandstone bodies are best exposed in the west-southwest portion of the study area where multiple north-northeast oriented sandstone bodies are present (Fig. 4.6A).

The overlying interval, interval 2, contains the first evidence of medium-width sandstone bodies. Sandstone bodies in interval 2 are characterized by their greater relative widths (e.g., 85 m), southeast trends, and low-sinuosity (Fig. 4.12B). The best example of these deposits are in the western portion of the study area, where a relatively wide, southeast-trending sandstone body cross-cuts and lies above the more narrow sandstone bodies of Interval 1 (Fig. 4.11). Here, paleocurrent directions vary almost 180 degrees between the sandstone bodies in interval 1 and 2.

Interval 3 is relatively poorly preserved throughout the study area, but where present are characterized by relatively narrow and somewhat sinuous sandstone bodies (Fig 4.12C). This interval is best exposed in the south-central portion of the study area (Fig 4.6A and Fig. 4.8A), where a narrow (44 m) ribbon sandstone body contains arcuate outer borders suggesting laterally migrating channels.

The uppermost interval, interval 4, is *not* the uppermost portion of the Salt Wash Member, but represents the uppermost interval with sufficient preservation for planview characterization. Interval 4 is characterized by several medium width (85 m), east trending, low-sinuosity sandstone bodies (Fig. 4.12D). These are best preserved in the north-central portion of the study area where three, relatively straight sandstone bodies cross-cut one another (Fig. 4.6A).

4.5.3.2. Discussion

We use the vertical position of the sandstone bodies as a proxy for the relative timing of deposition in this area. Rivers with relatively narrow, sinuous, northeast-flowing channels occupied the area initially, and were later replaced by southeast-flowing channels that deposited relatively wider channel belts. North-northeastern flowing river channels returned for a period, but were subsequently replaced by easterly flowing channels with similar characteristics to those found in interval 2. Throughout this entire cycle, crevasse splays occurred, recorded by very narrow sandstone bodies.

The vertical succession observed in our study area is consistent with recent DFS models. In prograding DFS, distal fine-grained deposits are overlain by coarser-grained medial and proximal sediments. The vertical trend is hypothesized to include a lowermost portion with mudstone-dominated facies and rare, isolated sandstone, an intermediate portion with mudstone and isolated to amalgamated fluvial sandstone bodies, and an uppermost portion with relatively coarse-grained, amalgamated fluvial sandstones with relatively little mudstone (e.g., Horton and Decelles, 2001; Nichols and Fisher, 2007; Hartley et al., 2010; Owen et al., 2015b, 2015c). The Morrison Formation in this area contains a lowermost portion dominated by clay- and siltstone paleosols with relatively thin (<3 m) sandstone bodies, some of which belong to the Tidwell Member. The Salt Wash Member strata exposed in our study area are smaller in the basal most layer (interval 1) and the largest sandstone bodies are in the upper most (preserved) intervals (interval 4). The change between narrow-width

sandstone bodies to medium-width sandstone bodies occurs through alternating intervals and not in sharp break, which may be more characteristic of DFS deposits in detail. The uppermost beds of the Salt Wash Member in our study area are also the coarsest-grained, with coarse-grained sandstone and beds of pebble-conglomerates. Where present these units are laterally continuous and intervals of mudstones are lacking; however due to their position in the succession these units are poorly preserved. We posit that these remains of the uppermost part of the Salt Wash Member represent the uppermost facies in the DFS model, which includes the amalgamated sandstone bodies.

4.5.4. Barform feature

4.5.4.1 Description

The southwestern portion of the study area contains evidence of a laterally migrating barform (Fig. 4.13A). The northern margin of the sandstone body is convex to the north and the southern boundary is limited by a cliff face. Grain size is dominantly medium grained with no noticeable trends across the exposure. The radius of curvature ranged between 66 and 116 m with an average of 94 m. Paleocurrent data indicate average flow was to the east (87°; n=173), but varied considerably, with values between 345° and 173°. The width of the exposure varies as a result of the arcuate northern margin of the sandstone, with values of 56 m in the west, 115 m in the center, and 65 m in the east. The majority of the surfaces within the sandstone body are convex-northward, similar in trend to the northern boundary, with the exception of one architectural element in the west-central area, which trends to the northwest-

southeast (Fig. 4.13B). The northernmost portion of the sandstone is composed of a single-story, asymmetric sand-filled channel with poorly developed lateral accretion surfaces. A series of west-east and northwest-southeast trending curvilinear sandstone bodies and surfaces are present in the east-central area, which based on their orientation, outward dipping surfaces, and related paleocurrent data are lateral accretion sets (Fig. 4.13C). These surfaces are much better preserved and represented on the downstream side of the exposure (Fig. 4.13D).

Mapping the accretion sets and determining the changes in sinuosity and radius of curvature allow us to infer channel pattern evolution (Fig. 4.14A-F). The southernmost bed has a sinuosity of 1.02, indicating a straight channel forming at the early stage of bend migration. Sinuosity shows a steady increase from successive accretion sets to the outer sandstone body with a sinuosity of 1.25. The radius of curvature for each accretion set shows a similar progression ranging from 66 to 116 m. Additionally, the apex of each of the bends shows a consistent shift to the northeast.

Measured sections were collected along the southern cliff face to characterize the vertical facies and architecture of this sandstone body (Fig. 4.15). The facies consist of trough and planar cross-stratification, granular sandstone, massive siltstone and sandstone, and red, green, and purple mottled mudstone. Sets of planar and cross-stratification commonly contain granular clasts at their base. Across much of the downstream length of the exposure (based on paleocurrent data), is a prominent erosional surface that extends

diagonally across the exposure. This surface is sharp and overlain by rip-up clasts of green mudstone. Overall, the vertical logs reveal a fairly uniform grain size sequence with slight fining upward intervals dominated by trough-cross-stratification with interbedded granules.

4.5.4.2. Paleohydraulic calculations

The preservation of the channel width, meander amplitude, and wavelength can be used to compare to values predicted by commonly used paleohydraulic equations (Table 4.1, Fig. 4.16). Preserved channel width was measured using the orthomosaic from the northernmost periphery and ranged between 13 and 23 meters with an average of 17 m ("preserved" width); this preserved width was multiplied by 1.5 to obtain an approximation of "true" width at bankfull stage (Allen, 1965; Moody-Stuart, 1966). Allen's (1965) equation and Moody-Stuart's (1966) conversion factor for asymmetrical meandering channels resulted in a true channel width ranging from 19.5 to 34.5 m with an average of 25 m. The preserved width and true width were used as inputs to calculate the meander wavelength and amplitude using equations from Leopold and Wolman, (1960). These were then compared to measurements extracted from the orthomosaic to see whether using a "preserved" or "true" width gave closer approximations.

The meander wavelength from the orthomosaic is 323 m (Fig. 4.16). The meander wavelength calculated by the 'preserved width' is 147 to 261 m with an average of 191 m. The meander wavelength predicted by the 'true width' of the channel is 221 to 394 m with an average of 288 m. The meander amplitude from

the orthomosaic is 101 m. The meander amplitude predicted by the 'preserved width' is 51 to 96 m with an average of 68 m. The meander amplitude predicted by the 'true width' is 79.8 to 149.5 m with an average of 106 m. In both instances using Allen's (1965) equation and Moody-Stuart's (1966) conversion factor resulted in more accurate representations of meander wavelength and amplitude.

4.5.4.3. Discussion

Based on the overall morphology, sedimentary characteristics, and paleocurrent data, we interpret this sandstone body as the deposit of a laterally migrating point bar (meandering river) that also records minor downstream (east) translation. The orientation of the accretion sets in planview, as well as the vertical architecture, suggest the barform accreted both laterally (to the north) and downstream (to the east), relative to the dominant paleoflow direction. This is also evident from the planview exposure where the apex of the bend surfaces shift farther northeast indicating an expansional evolution, similar to characteristics of Wu and Bhattacharya (2015) (Fig. 4.14). In addition, the poor preservation of the upstream deposits (western side) has been shown to be a characteristic feature of downstream migration (e.g. Ielpi and Ghinassi, 2014).

4.5.5. Salt Wash DFS and Modern Analog

4.5.5.1. DFS Models

The Salt Wash Member is arguably the best example of an ancient DFS, or fluvial megafan (Tyler and Ethridge, 1983; Weissmann et al., 2010; Owen et al., 2015c). Such features are increasingly recognized as important components of clastic depositional systems in basins (Hartley et al., 2010; Weissmann et al.,

2010, 2013), but sedimentary details from these deposits are scarce. A modern DFS is defined by: 1) channels that radiate from an apex; 2) a decrease in channel size and abundance downstream; 3) an increase in preservation of floodplain deposits relative to channel deposits downstream; 4) a decrease in grain size downstream; and 5) a change from amalgamated channel deposits in proximal areas to smaller fixed channels in distal areas (Horton and Decelles, 2001; Nichols and Fisher, 2007; Hartley et al., 2010; Weissmann et al., 2010).

The apex of the Salt Wash DFS exited paleotopography in northern Arizona/southern Utah (e.g., Owen et al., 2015a), implying our study area in central Utah was located in the medial zone of the DFS system. Models predict deposits in the medial zone of a DFS should include interstratified paleosol mudstone or lacustrine deposits, and fluvial sandstones deposited by anastomosing, meandering, and braided systems (Singh et al., 1993; Horton and Decelles, 2001; Owen et al., 2015c). Overall, the strata in the Salt Wash Member are consistent with predictions for medial zone DFS deposits. Strata are characterized by single- to multiple-story fluvial sandstone bodies deposited by straight to slightly sinuous channels, consistent with numerous DFS models (e.g. Nichols and Fisher, 2007; Cuevas Martínez et al., 2010; Owen et al., 2015c). The sandstone bodies are separated by laterally traceable mudstone intervals, such that the overall sandstone-mudstone ratio is between approximately 40-70%, which is also consistent with existing models (Owen et al., 2015c).

Salt Wash Member deposits in the study area contain characteristics that are not predicted by current, regional-scale models. All DFS models implicitly or

explicitly predict sandstone body orientations and paleocurrents in medial zones will be oriented roughly parallel to sub-parallel with the direction of the longitudinal length of the DFS (Singh et al., 1993; DeCelles and Cavazza, 1999; Horton and Decelles, 2001; Nichols and Fisher, 2007; Hartley et al., 2010; Owen et al., 2015c); in the case of the Salt Wash DFS, this direction is to the northeast (Tyler and Ethridge, 1983; Weissmann et al., 2013; Owen et al., 2015a, 2015c). Whereas the compiled paleocurrent data and sandstone body orientations are consistent with this prediction, in detail, the planview architecture is significantly more variable than predicted. The orientation of deposits associated with floodplain channels and crevasse splays (very narrow sandstone bodies) are expected to differ from the general trend, but variability is also present between narrow- and medium-width sandstone bodies, recording widely-oriented fluvial channels. Sandstone bodies with orthogonal or opposing paleocurrents and orientations are not part of current DFS models. At regional scales, the trends predicted by DFS models are likely accurate; however, our data suggests that at local scales (e.g., 10 km^2) these predictions are oversimplified. This variability could have important implications for understanding fluid behavior in petroleum reservoirs and aquifers.

4.5.5.2. Modern Analogue

Modern DFS are located around the globe (Leier et al., 2005; Hartley et al., 2010; Weissmann et al., 2011) and help serve as modern analogues for ancient deposits. The Bermejo Fan or DFS in northern Argentina is a relatively well-studied DFS, and like the Salt Wash DFS, it exits an actively deforming

retro-arc fold-thrust belt (Central Andes) and is deposited in the adjacent foreland basin (Chaco Plain) (Fig. 4.17) (Horton and Decelles, 2001; McGlue et al., 2016). In addition, the climate of the Bermejo DFS and its watershed is generally warm, tropical to semi-arid, and with seasonal discharge (Iriondo, 1993; Horton and DeCelles, 1997; Latrubesse et al., 2012; Weissmann et al., 2015; McGlue et al., 2016), which corresponds well to the reconstructed conditions of the Salt Wash DFS (Demko et al., 2004; Turner and Peterson, 2004; Myers et al., 2014).

The Salt Wash DFS deposits in our study area share several similarities to the fluvial deposits of the modern Bermejo DFS. The size of the Bermejo River channel is greater than the sandstone body width in the Salt Wash Member, but similar to the Salt Wash Member the Bermejo DFS contains channel deposits that range across several scales. The medial zone of the Bermejo DFS includes the principal trunk channel (the Bermejo River), smaller, abandoned, sinuous channels, and even smaller channels adjacent to the trunk channel (Fig 4.17B-D). The planview nature of the channels is highly variable, with evidence of meandering river systems, low-sinuosity non-migrating rivers, and portions of the trunk channel that are similar to braided stream channels. At the scale of our study area (~10 km^2), the orientation of these individual channels is variable, with 90° relationships common. The trunk channel of the Bermejo DFS contains ~km long stretches where it is straight and localized zones with point bars and meander bends. The straight portions of the channel are consistent, at least in appearance, with the low-sinuosity medium-width sandstone bodies in our study area. The presence of meander bends along the trunk channel suggest it is

possible the straight segments in our study area are only representing a portion of the ancient fluvial system and that these deposits may have characteristics more similar to meandering rivers in across a regional scale.

4.6. Summary and Conclusions

Planview exposures of the Upper Jurassic Salt Wash Member in east-central Utah allow for a relatively unique examination of ancient fluvial deposits. With field based observations, UAVs, and SfM data, we were able to characterize these deposits across a ~10km^2 area. Four dominant sandstone body types were documented based on size, orientation, and paleocurrent data. Very narrow sandstone bodies (4-6 m wide) are less than 2 m thick and heavily bioturbated. Narrow sandstone bodies (15 to 45 m wide) are straight to sinuous, contain evidence of lateral migration, and were deposited by north-northeast flowing fluvial systems. Medium sandstone bodies (75 to 130 m wide) are straight, and were deposited by non-migrating, east-flowing fluvial systems. Sheet/other sandstone bodies consist of both sheet-like sandstones whose edges are not visible and eroded sandstones bodies that cannot be reconstructed. These different sandstone body types reflect deposition by different types and sizes of fluvial channels. The average values of widths, sandstone body orientations, and paleocurrents do not adequately capture the variability in these parameters. Current DFS models, which are generally focused on regional-trends, also fail to predict the degree of variability at this scale. The sandstone bodies are highly variable with paleocurrents and orientations spanning > 180°. These differences suggest that large scale models may not be applicable to specific zones in DFS

deposits. While these models can act as a starting point to gain an understanding of regional trends, they fall short of being able to describe the true variability within these systems.

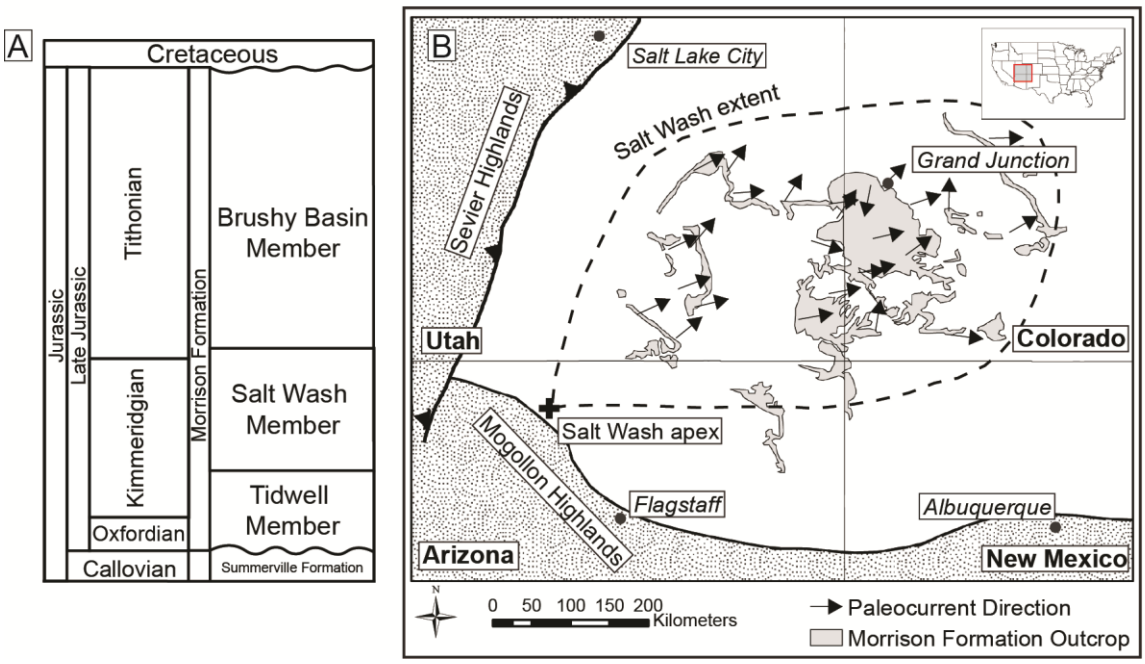

Figure 4.1. A) Stratigraphy of the Morrison Formation, modified from Owens et al. (2015c). B) Location map of the Salt Wash fluvial system. Salt Wash Member extent mapped out by Mullens and Freeman (1957). The apex position was defined by Owens et al. (2015a) (modified from Owens et al. (2015c)).

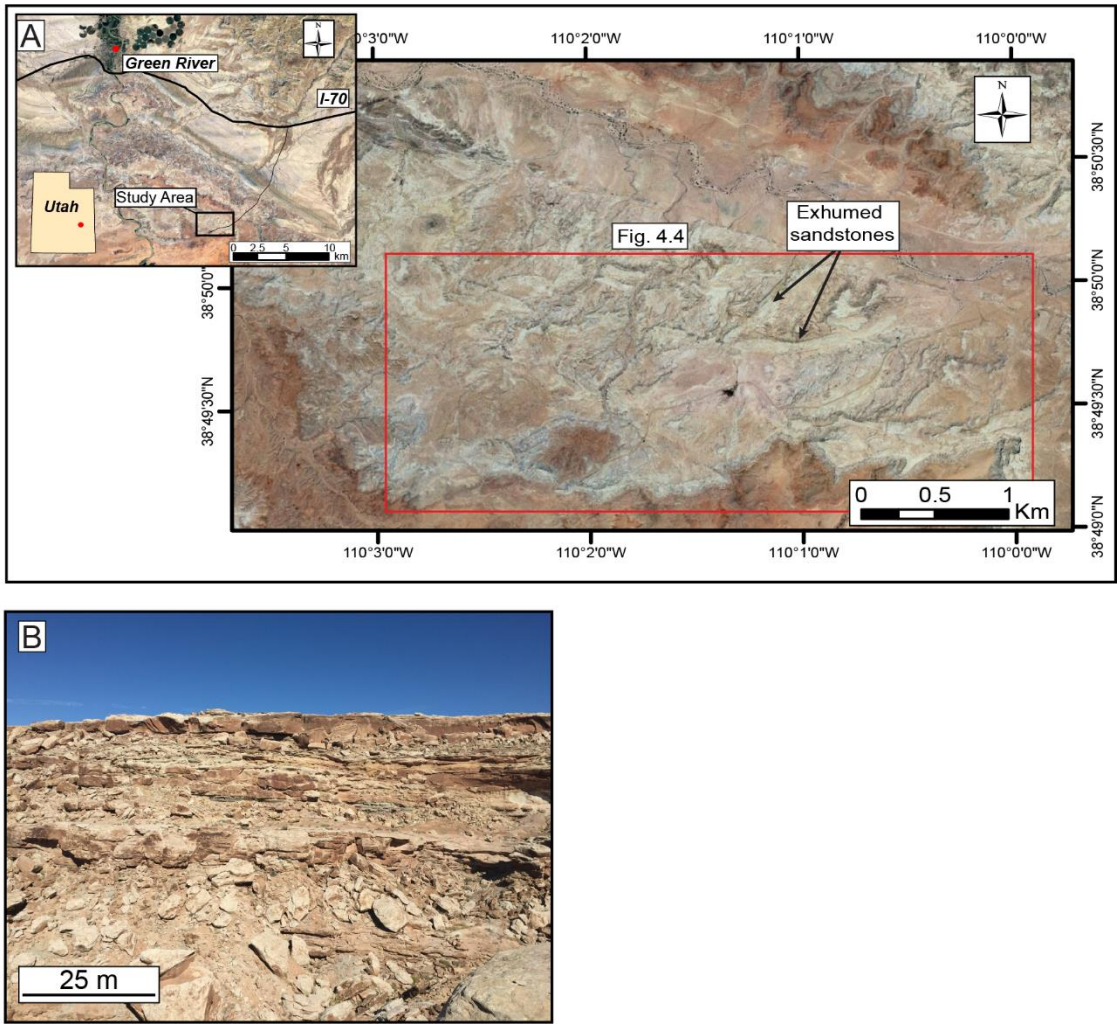

Figure 4.2. A) Imagery from Google Earth showing the study area, southeast of Green River, Utah. Exhumed sandstone bodies can be seen across much of the area. B) Vertical profile of the Salt Wash Member along the southern edge of the canyon.

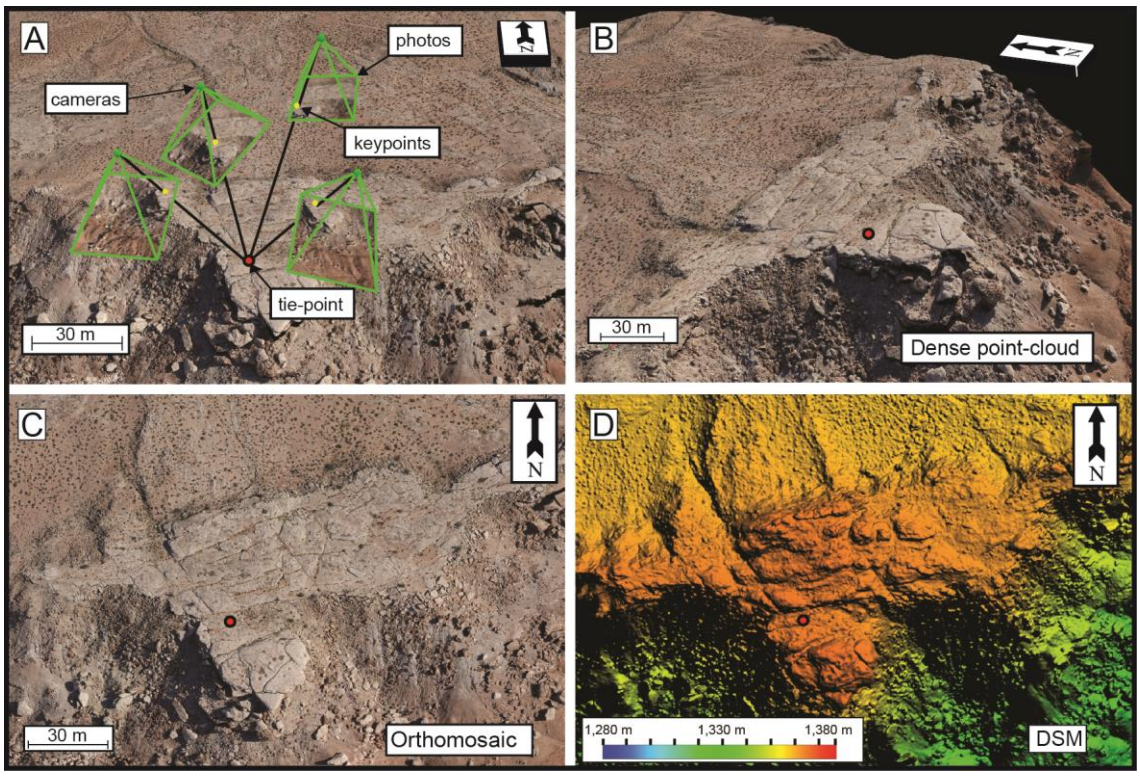

Figure 4.3 A) Structure-from-motion (SfM) photogrammetry concept. Green spheres represent camera locations, green squares show the digital images. The outcrop of interest is in the background. Multiple overlapping images are taken and a matching algorithm identifies keypoints in each image (yellow dots) and corresponding keypoints are matched between images. The location of those keypoints are triangulated and projected into a 3-D space (black ray traces) generating tie-points (red dot), creating a sparse 3-D point-cloud. Following this, a densified point-cloud B) and mesh are generated from the sparse-point cloud. The densified point-cloud and the calibrated images are used to obtain elevation information and remove perspective distortion to generate the orthomosaic and DSM (C and D).

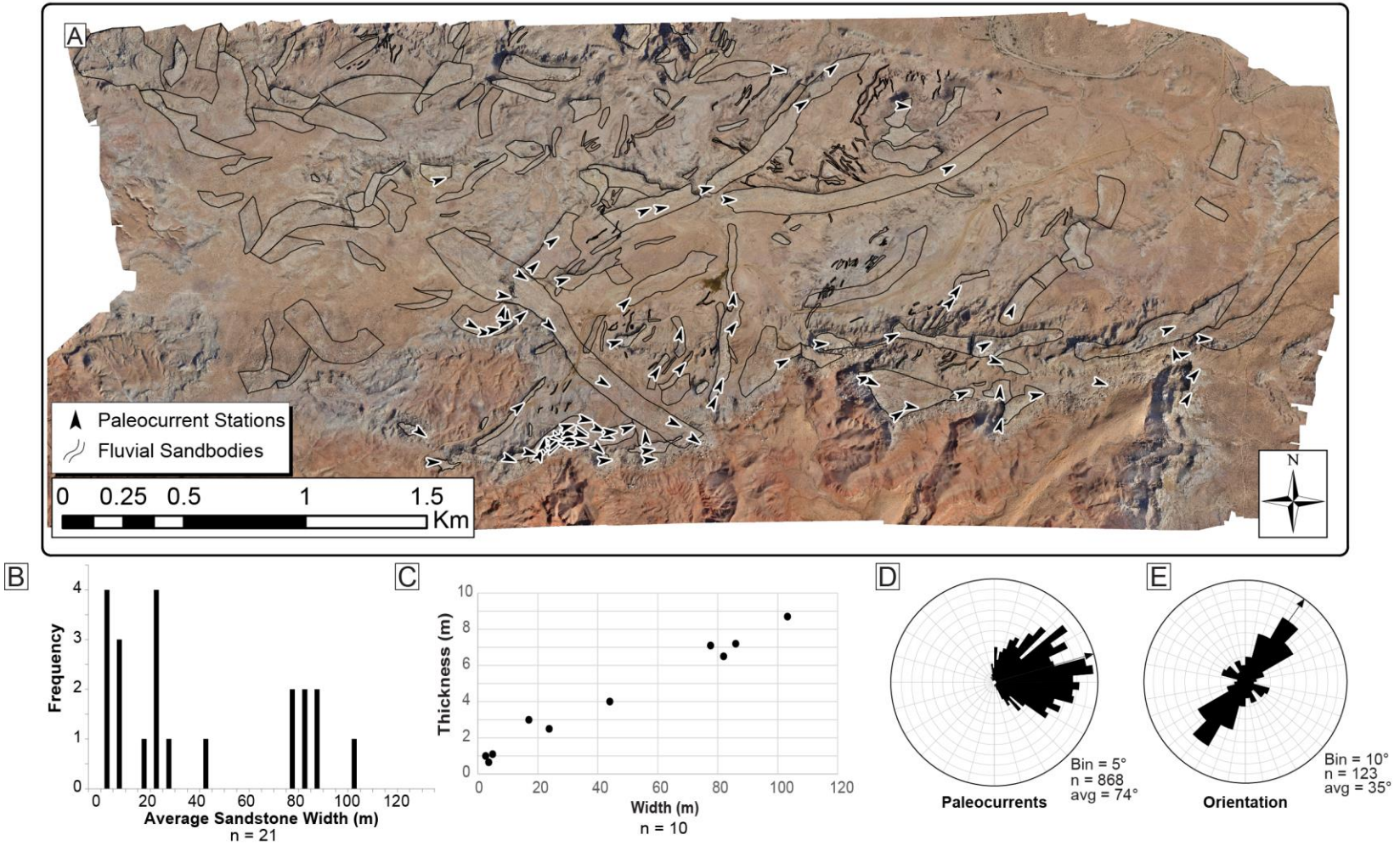

Figure 4.4. A) Overview of the study area with all mapped out fluvial sand bodies exposed in planview and paleocurrent directions. B) Average width distribution of the 21 sandstone bodies. C) Width/thickness (W/T) plots for the channel deposits in the Salt Wash Member exposed in planview. D and E) Rose diagrams for paleocurrents and sand body orientations. The dominant paleoflow direction is to the northeast, but ranges from north to southeast. The sandstone bodies are dominantly oriented to the northeast.

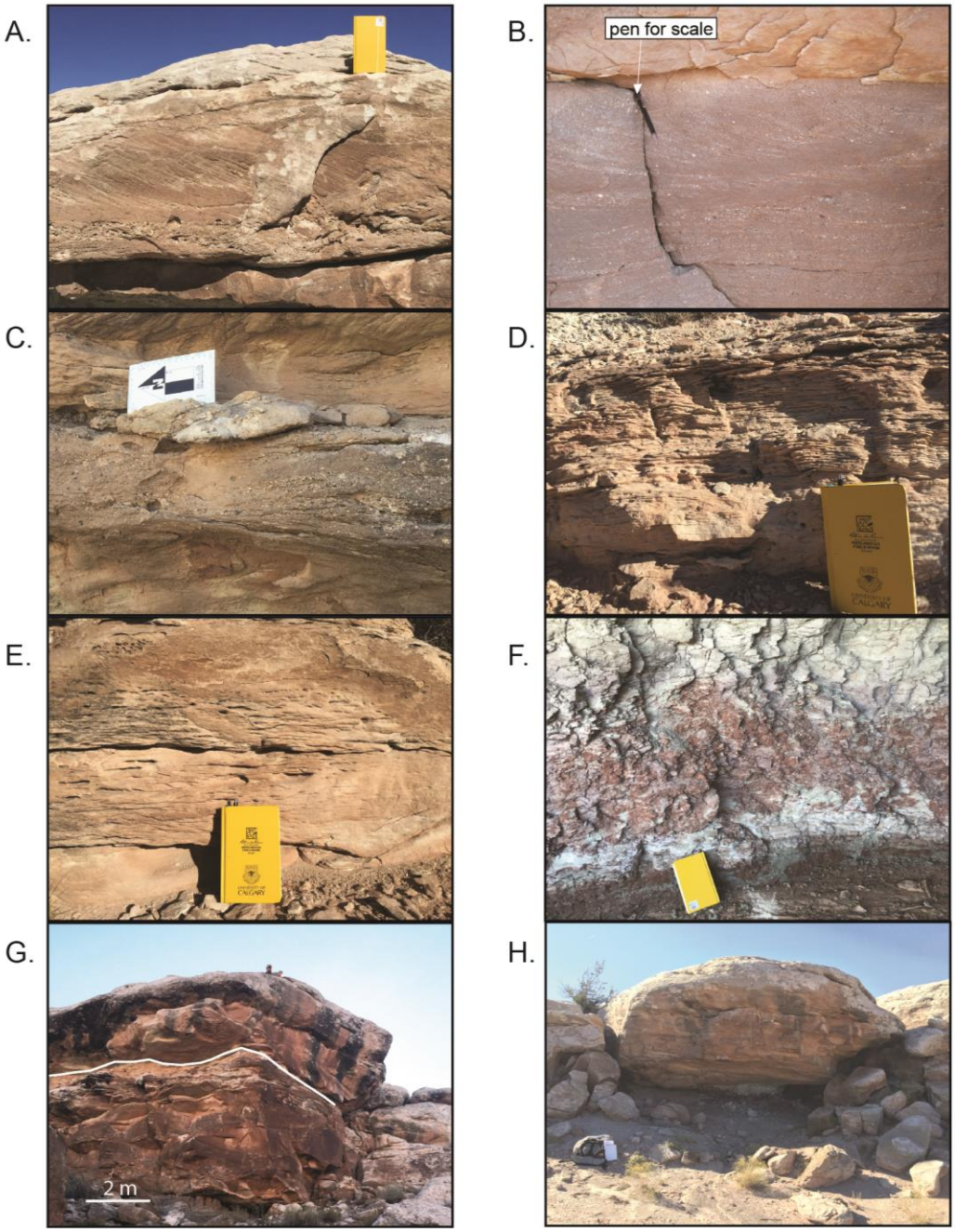

Figure 4.5. Illustrations of selected facies found from the Salt Wash Member in the study area. A) Medium to course grained planar cross-bedding. B) Medium to granular trough-cross bedding often pebble lags separating beds. C) Pebble conglomerates. D) Fine-grained planar laminated sandstone. E) Current rippled sandstone. F) Clay-rich paleosols. G) Multistory sandstone bodies. H) Single story sandstone bodies.

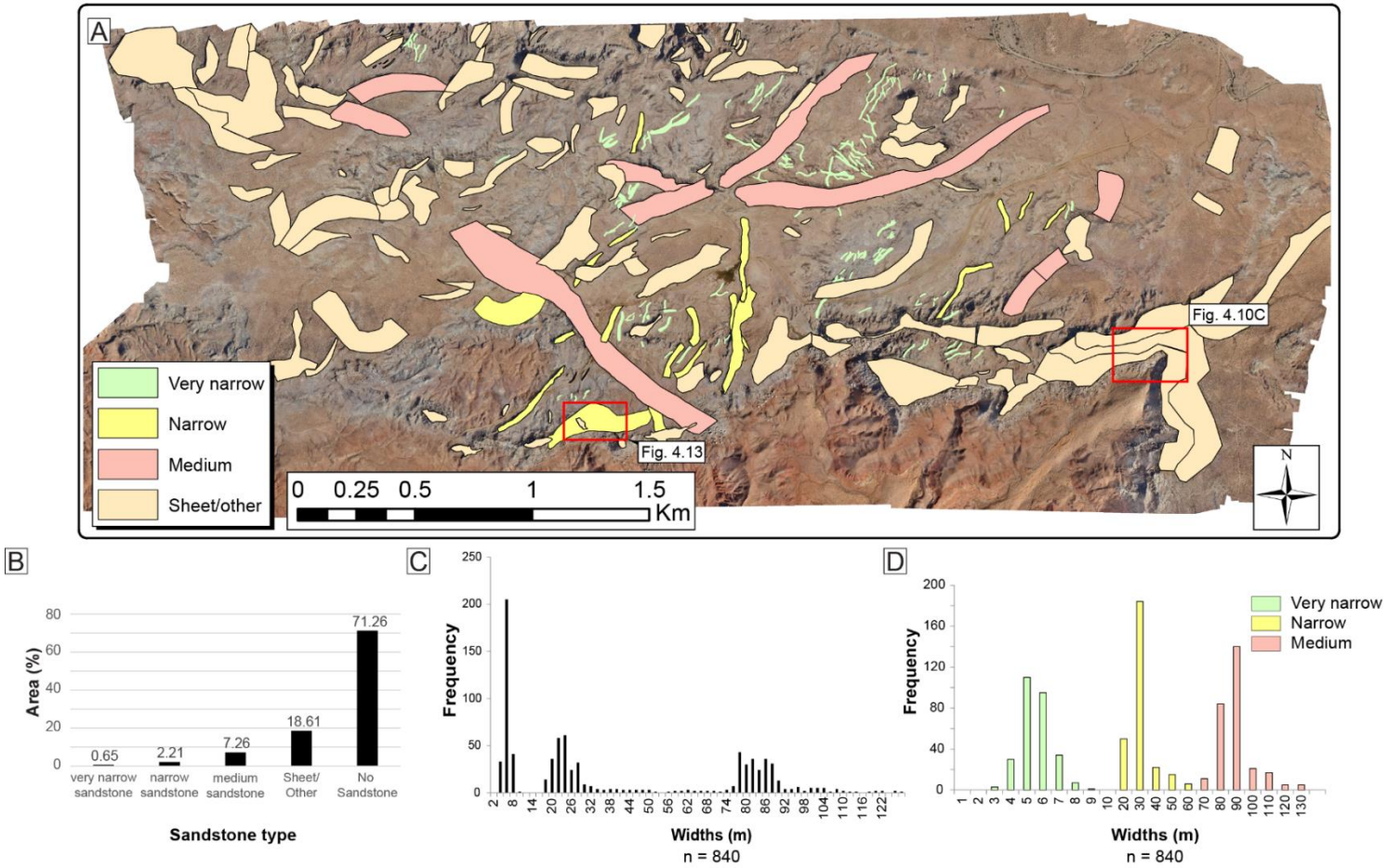

Figure 4.6. A) Study area with sandstone bodies categorized by color. B) Bar graph depicting the percentage of the total area for each type of deposit. C) Raw width measurements plotted on a frequency distribution graph. Three distinct peaks can be seen at < 10 m, 15-30 m, and 75-90 m. D) Widths plotted with a modified scale on the x-axis to highlight the three distinct sandstone body sizes found.

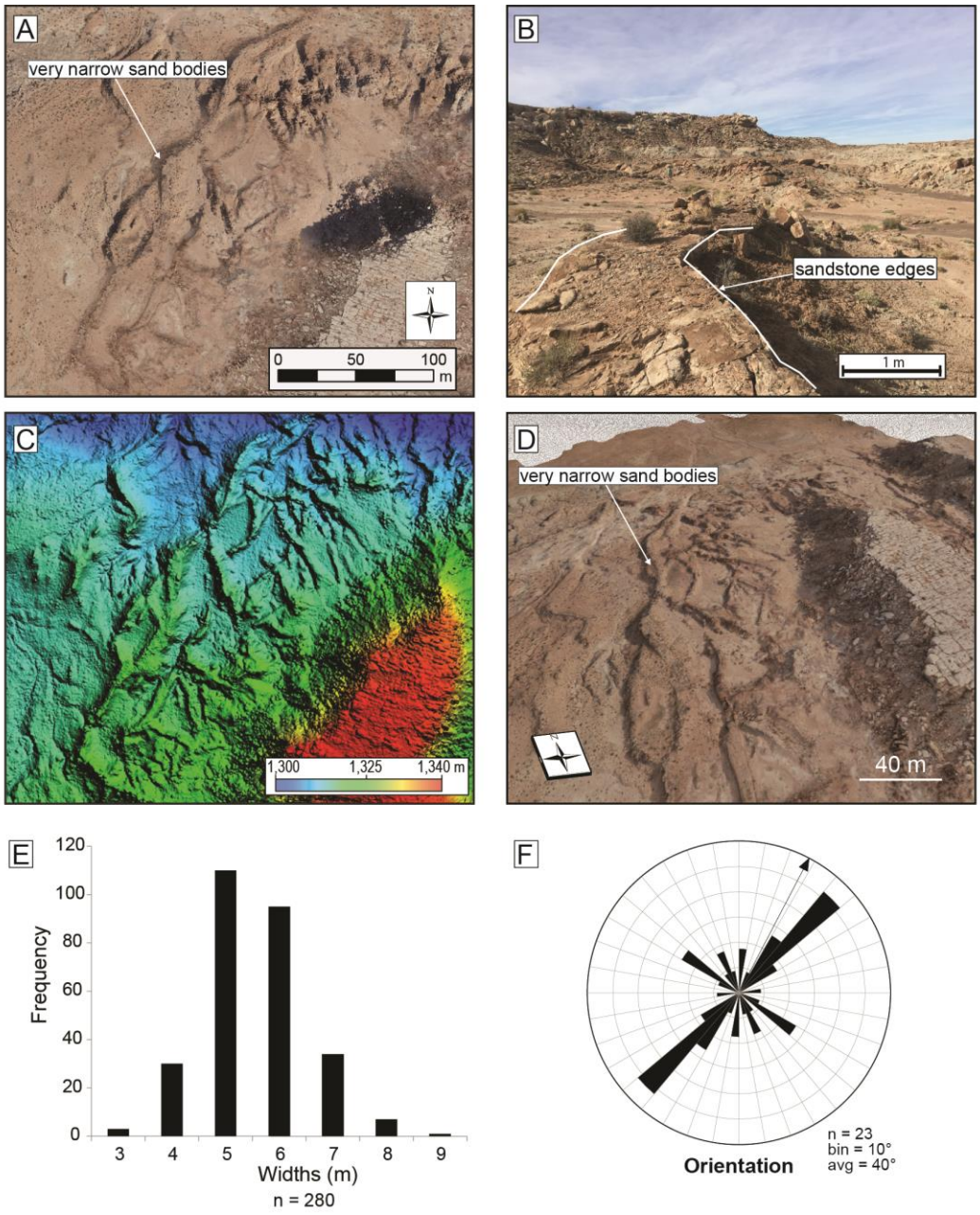

Figure 4.7. Very narrow sandstone bodies. A) Planview exposure of the very narrow sand bodies from the orthomosaic. B) Photograph taken from the ground showing the typical style and geometry. C) The DSM emphasizes the dendritic arrangement of these sandstone bodies. D) The mesh showing a perspective view of the deposits. E) Width distribution graph. F) Rose diagram showing the orientations of these sandstone bodies. While the average is oriented to the northeast, these show the greatest distribution of all the other exposed sandstone bodies.

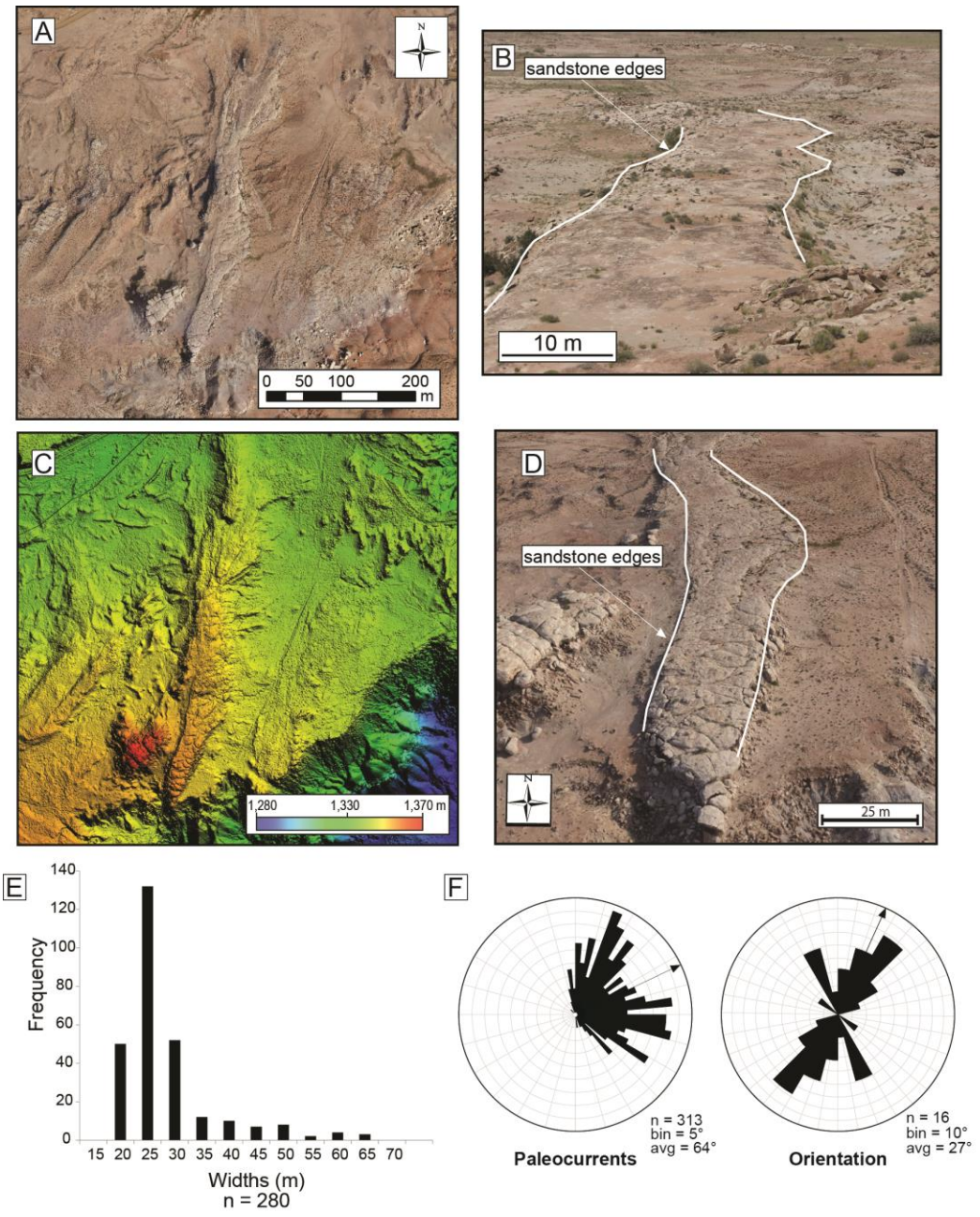

Figure 4.8. Narrow sandstone bodies. A) An example of one of these deposits with a northern orientation and flow direction from the orthomosaic. B) Photograph taken from the ground showing the typical style and geometry. The edges are highlighted by the white line. C) DSM of the exposures seen in A. D) Mesh showing a perspective view of the sandstone seen in A. E) Width distribution graph. Measurements range from 15 m to 65 m, with the largest concentration being between 20-30 m. F) Rose diagrams depicting the paleocurrent directions and orientations.

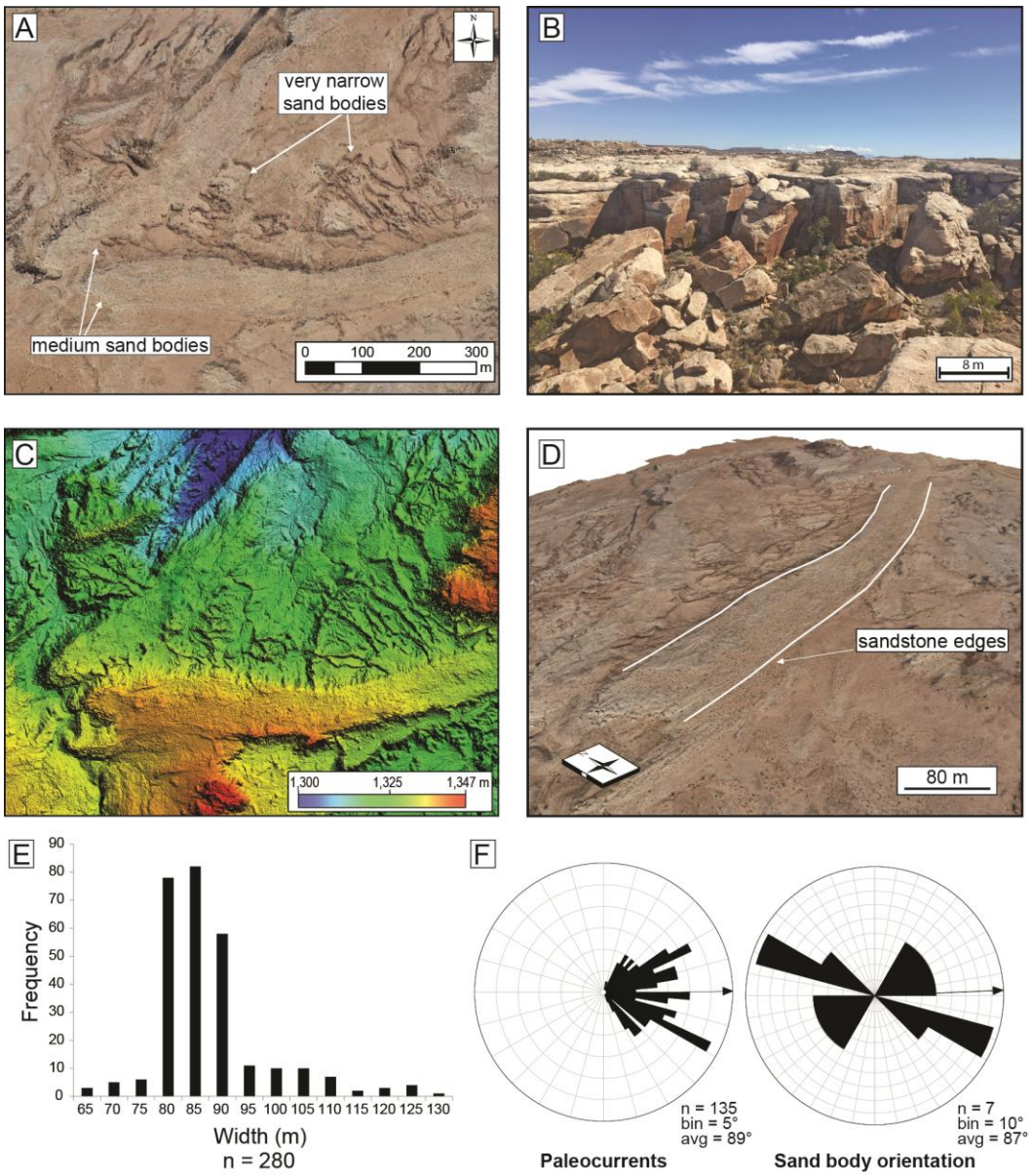

Figure 4.9. Medium sandstone bodies. A) Two medium sandstone bodies oriented to the northeast and east with corresponding paleocurrent directions. The very narrow sandstone bodies sit slightly under these deposits and show a general orientation perpendicular to the medium sandstone bodies. B) Photograph taken from the ground showing the profile of one of these deposits. They characteristically differ from the very narrow and narrow in thickness, lateral extent, and channel stacking behavior. C) The DSM of the sandstone bodies from A. D) The mesh surface showing the eastern oriented sandstone body in A. The preserved edges are traced in white. E) Width distribution graph. Measurements range from ≥65 m to 130 m, with the largest concentration being between 80-90 m. F) Rose diagrams depicting the paleocurrent directions and orientations.

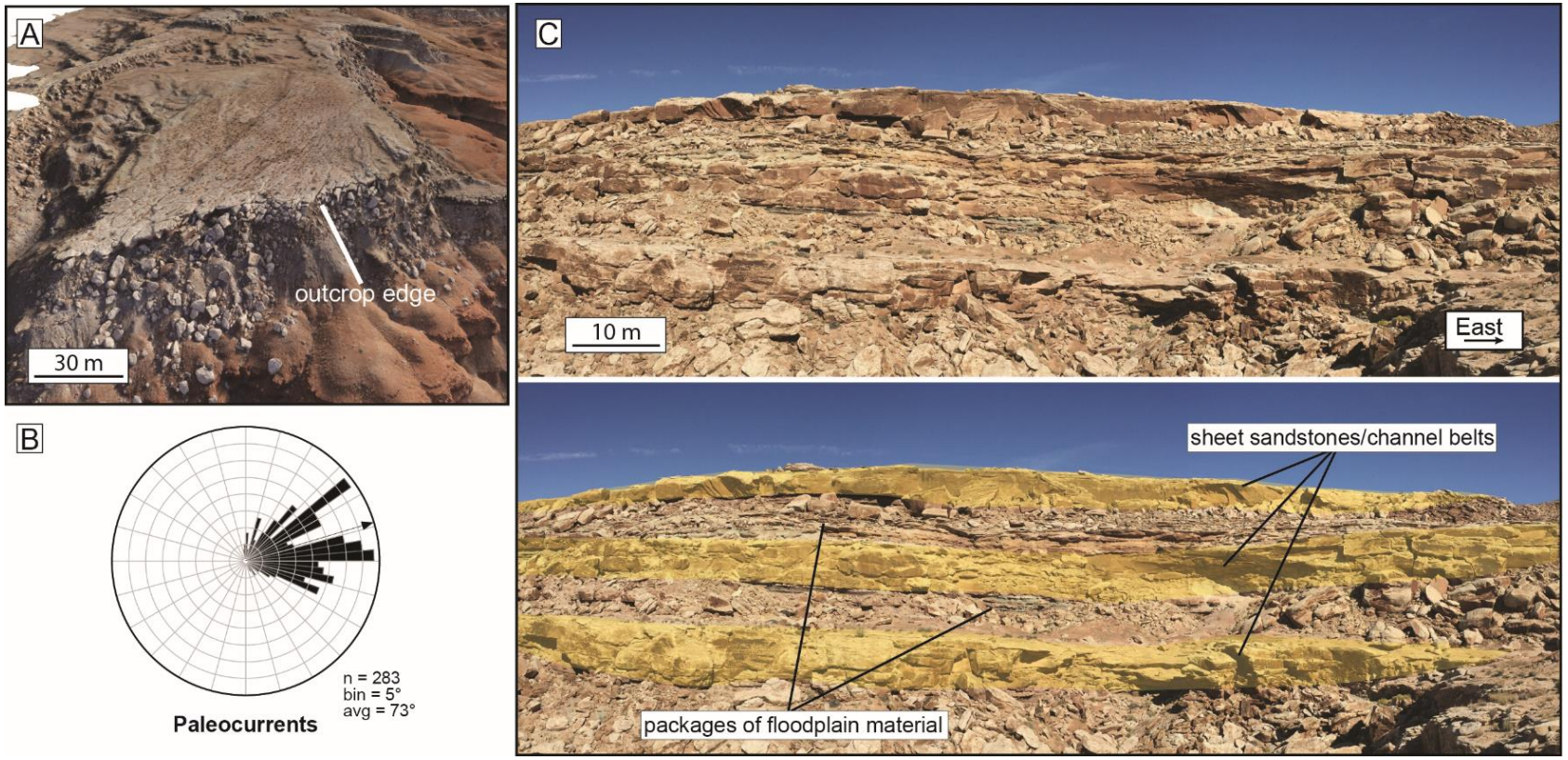

Figure 4.10. Sheet/other sandstone bodies. A) Perspective view of a sheet sandstone exposed along the southern margin. B) Rose diagram showing the paleocurrent trends for these exposures. C) Profile view showing the sheet/other sandstone bodies exposed along the canyon in the southern edge of the study area. Three distinct belts can be seen separated by packages of floodplain material. These are similar to deposits described by Owens et al. (2015c).

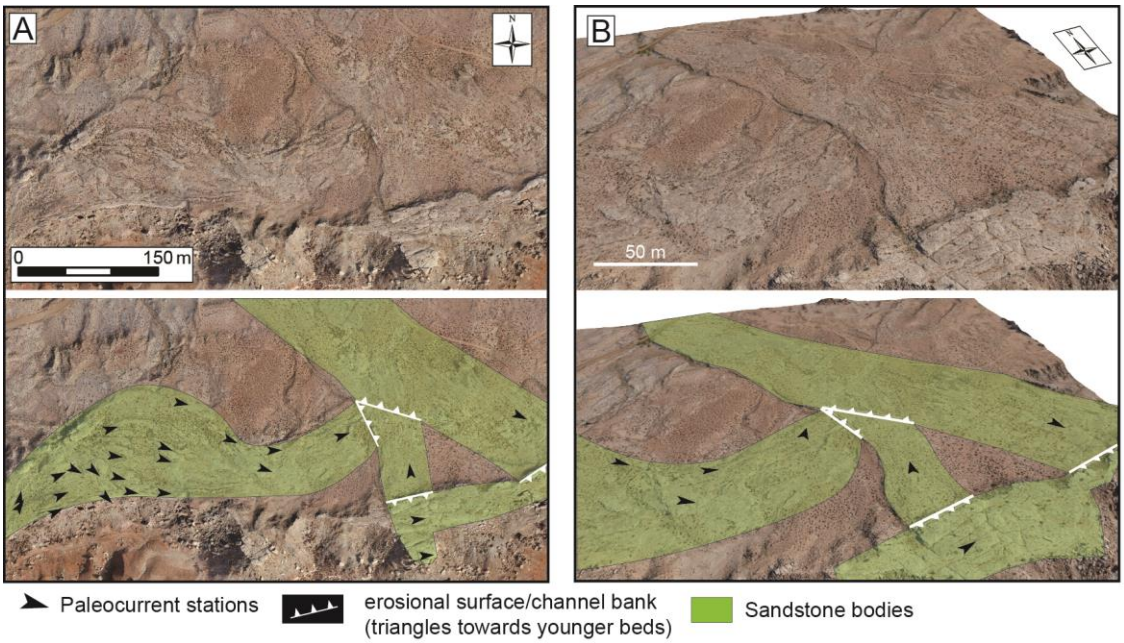

Figure 4.11. Example of cross-cutting relationships and superposition. A) The top image is a perfect example demonstrating the cross-cutting relationships between adjacent sandstone bodies. The bottom image is an interpreted depiction of these relationships. The lowermost unit is a laterally accreting barform that is overlain by a north trending sandstone body. This unit is then cut, by a larger southeast oriented sandstone body. Finally this unit is overlain by a smaller sandstone body oriented towards the east. B) Perspective view from the textured mesh of the same sandstone bodies in A.

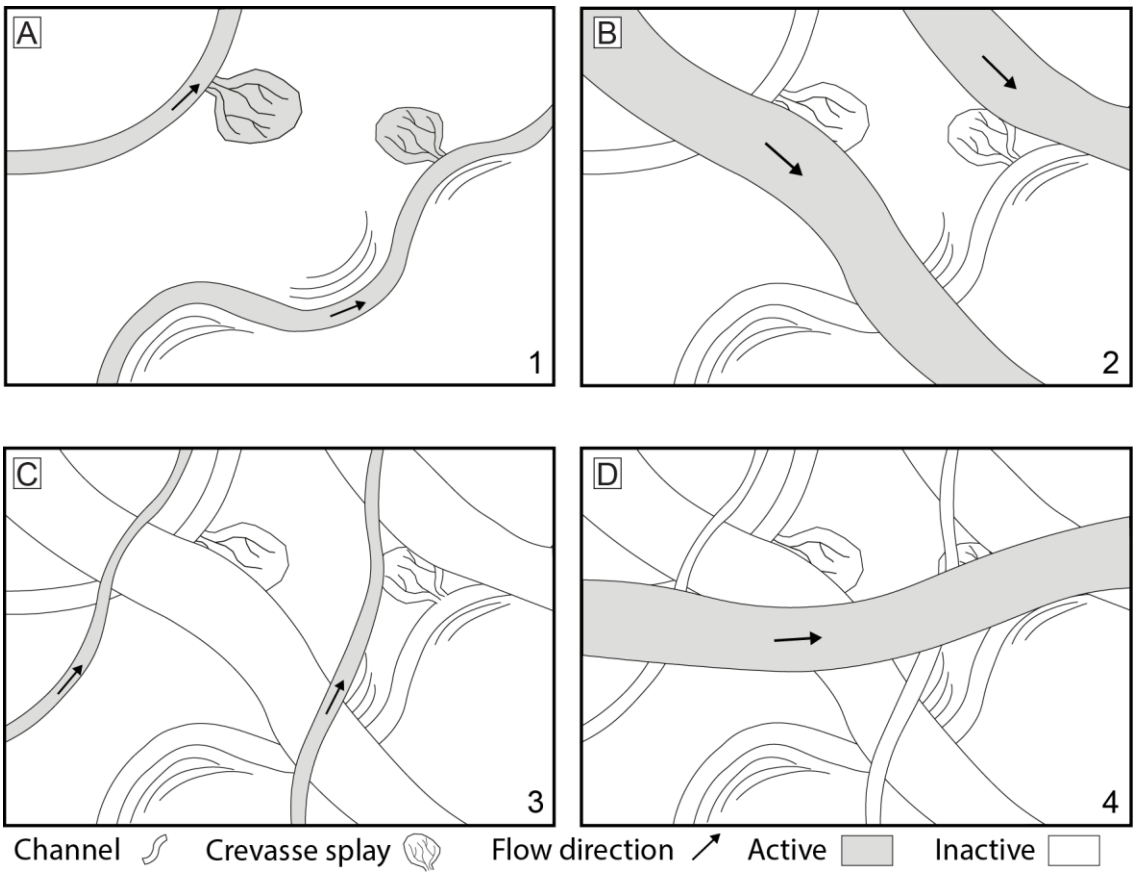

Figure 4.12. Schematic diagram showing the general evolution of vertical deposition. A) Interval 1 is characterized by narrow sandstone bodies and north-northeast trends. This is the only interval with conclusive evidence of point-bar deposits. B) Interval 2 is dominated by medium sandstone bodies and show a southeast orientation. These sandstone bodies are straight in nature with only slight evidence of lateral migration. C) Interval 3 is similar in channel style to interval 1, but show a stronger orientation to the north. D) Interval 4 is similar in channel style to interval 2, but the preserved sandstone bodies are oriented east-northeast.

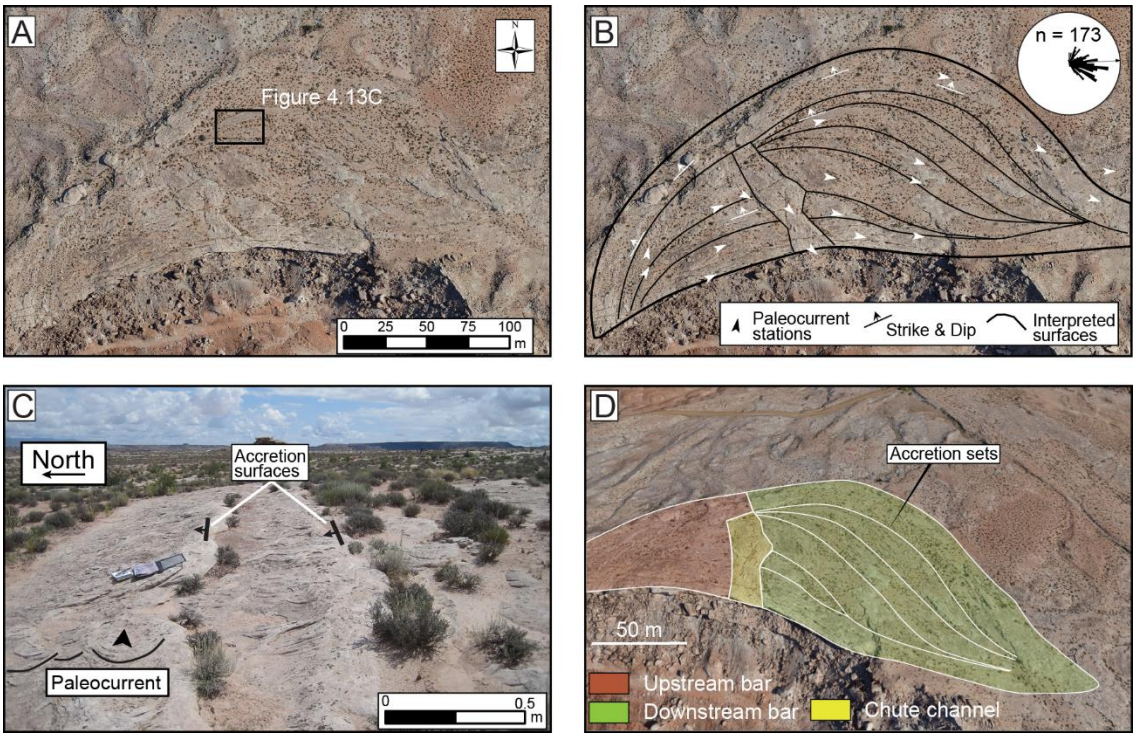

Figure 4.13. Barform feature (see Fig. 4.6 for location). A) Orthomosaic of the barform feature. B) Interpretation and data from the barform, derived from the UAV-SfM imagery and ground-based observations. Individual elements and the barform margins were mapped onto the orthomosaic. These interpretations were combined with paleocurrent and strike and dip data taken at multiple stations. Paleocurrent arrows represent the averages at each station. The geometry of the surfaces and ground-based data indicate the internal elements are accretion surfaces of a barform (point-bar) deposit. C) Photograph from the field showing an example of the accretion surfaces and the individual bars with paleocurrent indicators. D) Perspective view from the textured mesh showing the different sections of the barform. The upstream portion (red) does not display as prominent accretion surfaces as the downstream portion (green). A northwest-southeast architectural element can be seen cutting across the barform and has been interpreted as a chute channel that was deposited after the point-bar was in place.

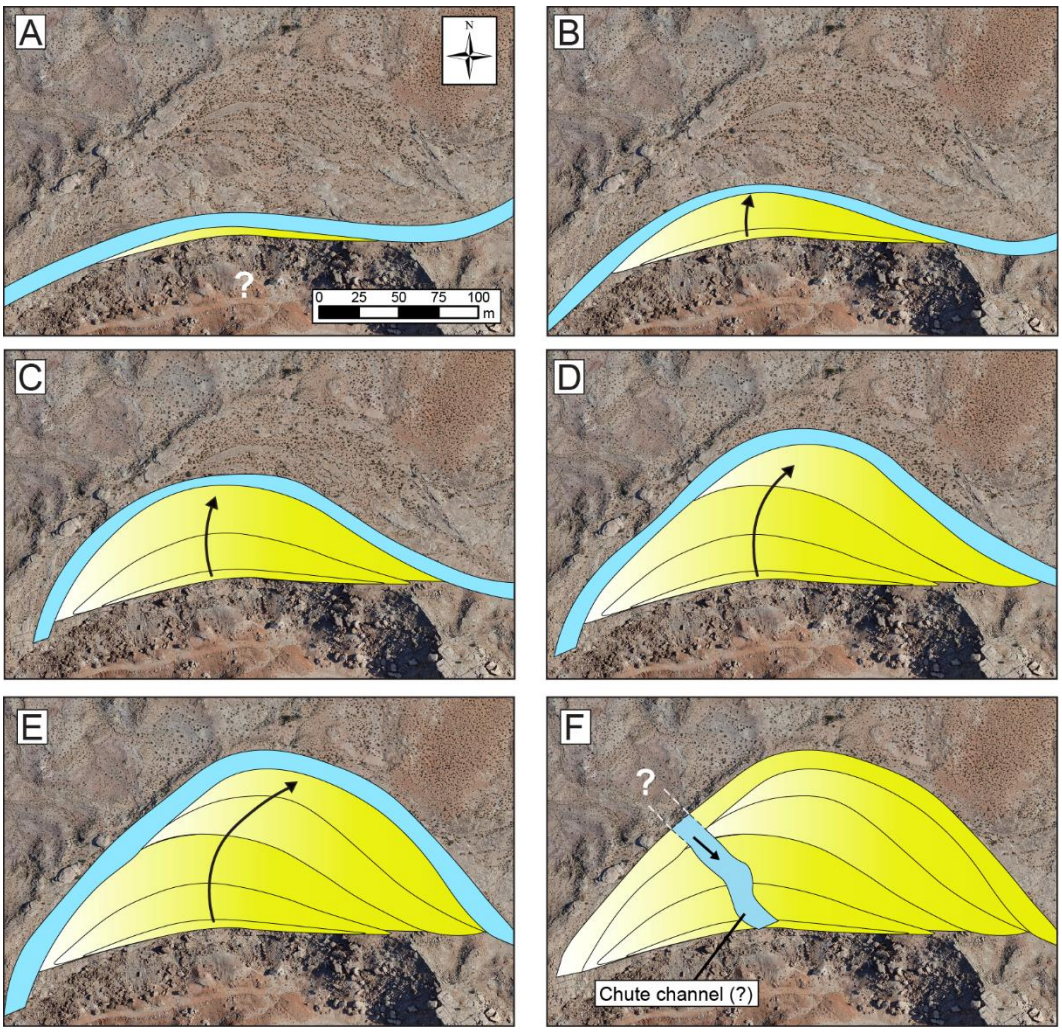

Figure 4.14. A-E) Schematic diagram showing the barform evolution based on the geometry of accretion sets and change in radius of curvature. The question mark represents areas of unknown due to erosion. The black arrow represents the direction of migration. A to C was dominated by laterally accretion to the north. D to E represent a change from a dominantly lateral to downstream migration. F) Southeast oriented sandstone body cuts across the accretion sets and may resemble a chute channel deposit. The dotted lines represent an inferred channel boundary.

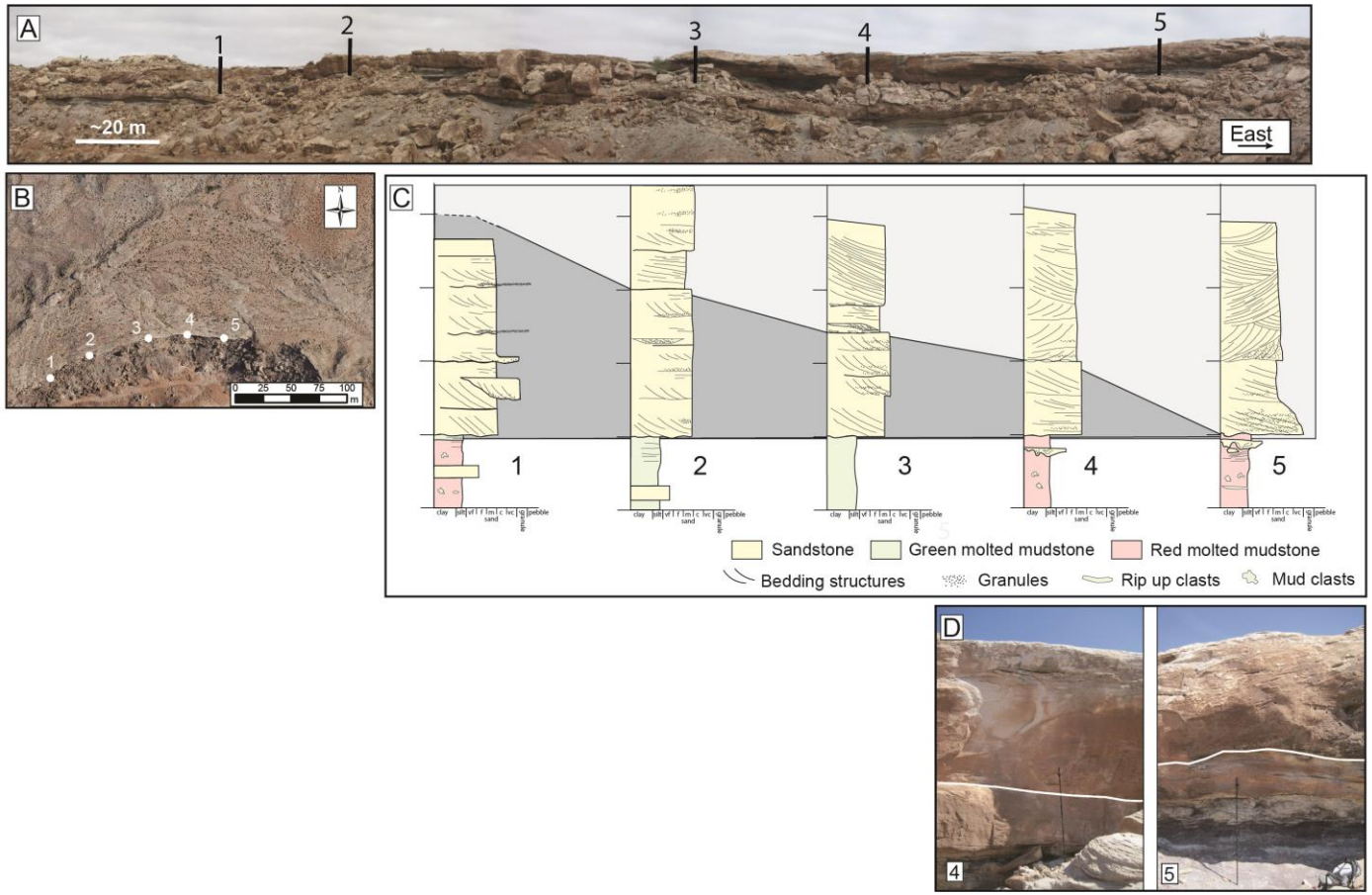

Figure 4.15. A) Photomosaic of the vertical exposure of the barform feature with the locations of the vertical logs. B) Orthomosaic of the barform feature with the locations of the vertical logs. C) Five vertical logs taken along the southern exposure of the barform feature. A prominent erosional surface can be traced across logs 2 to 5 and inferred from log 1. D) Two photographs taken from logs 4 and 5. The white line represents the erosional surface traced across the logs.

Table 4.1. Paleohydraulic equations and calculations.

Preserved Width				
	Paleohydraulic Equation	**Source**	**Avg (m)**	**Range (m)**
Width	width of outer sandstone	Orthomosaic	17	13-23
Meander wavelength	$Lm = 10.9 \times w_p^{1.01}$	Leopold and Wolman (1960)*	262	191-147
Meander amplitude	$Am = 2.7 \times w_p^{1.1}$	Leopold and Wolman (1960)*	68.0	51-96

True Width				
	Paleohydraulic Equation	**Source**	**Avg (m)**	**Range (m)**
Width	$w = 1.5 \times w_p$	Allen, 1965	25	20-35
Meander wavelength	$Lm = 10.9 \times w^{1.01}$	Leopold and Wolman (1960)*	288	222-394
Meander amplitude	$Am = 2.7 \times w^{1.1}$	Leopold and Wolman (1960)*	106	80-150

w - true width w_p - preserved width Lm - Meander wavelength Am - Meander amplitude
**values converted from imperial to metric*

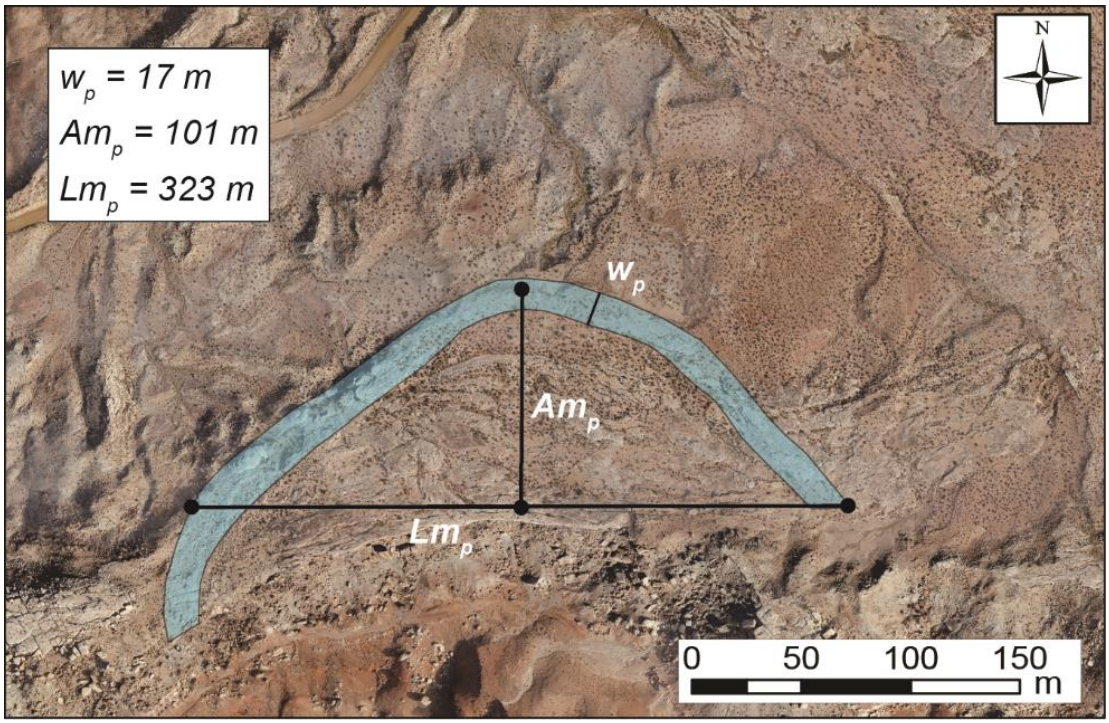

Figure 4.16. Paleohydraulic measurements taken from the orthomosaic.

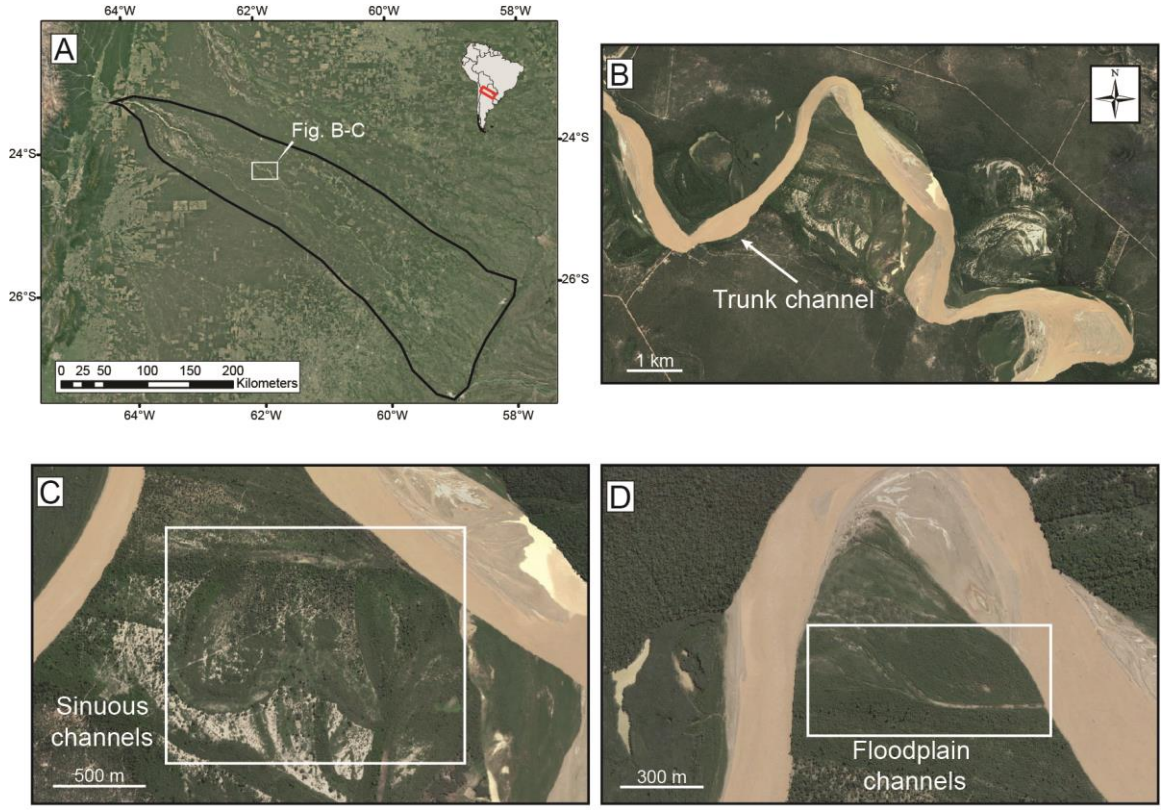

Figure 4.17. A) Location map of the Bermejo DFS. B) Trunk channel located in the medial region of the Bermejo DFS. These channels most closely represent the medium sized sandstone bodies within our study. C) Abandoned channels that show a high degree of sinuosity and meander bends. These abandoned channels are most similar to the narrow sandstone bodies within our study. D) Floodplain channels coming off of the main trunk channel seen in B. These channels are most similar to the very narrow sandstone bodies within our study area.

CHAPTER 5

CONCLUSION

The combined use of UAVs and SfM photogrammetry provides an effective way to acquire data from sedimentary outcrop exposures. This method is particularly useful for intermediate-scale features and helps bridge the gap between existing aerial imagery and ground-based observations. In addition, SfM records the 3-D nature of outcrops, making it perfect for capturing complicated exposures. The use of UAVs in image acquisition allows larger areas to be studied without losing detail, including exposures that are inaccessible by foot (e.g., vertical cliff faces). Although it should be tested prior to use, the 3-D reconstructions made from UAV-SfM can achieve a relative accuracy to a sub-meter scale and can be used to gather quantitative data from outcrop exposures. That being said, this method is not without limitations. In terms of quality, TLS data yield far higher resolution and show more consistency relative to SfM (Wilkinson et al., 2016). The prices of UAVs are decreasing, but such devices are not without initial costs and many require operator training before use. In addition, UAVs cannot be used everywhere; UAVs are regulated by federal and local agencies, which should be consulted prior to their use. Despite these drawbacks, the combined use of UAVs and SfM photogrammetry represents a promising new tool for characterizing and studying sedimentary outcrops.

Integrating a light-weight UAV and SfM photogrammetry with field-based measurements and observations this study illustrates the variability that can exist within preserved fluvial systems. All current DFS models predict sandstone bodies and paleocurrents in proximal and medial zones should be oriented roughly parallel to sub-parallel with the direction of the radial length of the DFS (Singh et al., 1993; DeCelles and Cavazza, 1999; Horton and Decelles, 2001; Nichols and Fisher, 2007; Hartley et al., 2010; Owen et al., 2015c). In the case of the Salt Wash DFS, this direction is to the ~northeast (Tyler and Ethridge, 1983; Weissmann et al., 2013; Owen et al., 2015a, 2015c). Whereas the compiled paleocurrent data and sandstone body orientations are consistent with this prediction, in detail, the orientation of sandstone bodies and paleocurrents is much more varied than predicted. Within the study area defined in Chapter 4, these sandstone bodies are highly variable with paleocurrents and orientations spanning > 180°. These differences suggest that large-scale models may not be applicable to specific localities in DFS deposits. While these models can act as a starting point to gain an understanding of regional trends, they fall short of being able to describe the true variability within these systems. Thus, an important step forward will be to place an emphasis on studying fluvial deposits exposed in planview to better understand the variability that exists within larger scale depositional systems and their associated models.

REFERENCES

Allen, J.R.L., 1965. The sedimentation and palaeogeography of the Old Red Sandstone of Anglesey, north Wales. Proceedings of the Yorkshire Geological Society 35, 139–185. doi:10.1144/pygs.35.2.139

Bellian, J. a., Kerans, C., Jennette, D.C., 2005. Digital Outcrop Models: Applications of Terrestrial Scanning Lidar Technology in Stratigraphic Modeling. Journal of Sedimentary Research 75, 166–176. doi:10.2110/jsr.2005.013

Bemis, S.P., Micklethwaite, S., Turner, D., James, M.R., Akciz, S., T. Thiele, S., Bangash, H.A., 2014. Ground-based and UAV-Based photogrammetry: A multi-scale, high-resolution mapping tool for structural geology and paleoseismology. Journal of Structural Geology 69, 163–178. doi:10.1016/j.jsg.2014.10.007

Best, J.L., Ashworth, P.J., Bristow, C.S., Roden, J., 2003. Three-Dimensional Sedimentary Architecture of a Large, Mid-Channel Sand Braid Bar, Jamuna River, Bangladesh. Journal of Sedimentary Research 73, 516–530. doi:10.1306/010603730516

Bistacchi, A., Balsamo, F., Storti, F., Mozafari, M., Swennen, R., Solum, J., Tueckmantel, C., Taberner, C., 2015. Photogrammetric digital outcrop reconstruction, visualization with textured surfaces, and three-dimensional structural analysis and modeling: Innovative methodologies applied to fault-related dolomitization (Vajont Limestone, Southern Alps, Italy). Geosphere 11, 2031–2048. doi:10.1130/GES01005.1

Bridge, J.S., Alexander, J., Collier, R.E.L., Gawthorpe, R.L., Jarvis, J., 1995. Ground-penetrating radar and coring used to study the large-scale structure of point-bar deposits in three dimensions. Sedimentology 42, 839.

Bridge, J.S., 2006. Fluvial facies model: recent developments, in: Posamentier, H.W., Walker, R.G. (Eds.), Facies Models Revisited. SEPM Special Publication, pp. 85–170.

Bristow, C.S., 1987. Brahmaputra River: Channel Migration and Deposition, in: Recent Developments in Fluvial Sedimentology. SEPM Society for Sedimentary Geology, pp. 63–74. doi:10.2110/pec.87.39.0063

Buckley, S.J., Howell, J.A., Enge, H.D., Kurz, T.H., 2008. Terrestrial laser scanning in geology: data acquisition, processing and accuracy considerations. Journal of the Geological Society 165, 625–638. doi:10.1144/0016-76492007-100

Buckley, S.J., Enge, H.D., Carlsson, C., Howell, J.A., 2010. Terrestrial laser scanning for use in virtual outcrop geology. Photogrammetric Record 25, 225–239. doi:10.1111/j.1477-9730.2010.00585.x

Carter, D.C., 2003. 3-D seismic geomorphology: Insights into fluvial reservoir deposition and performance, Widuri field, Java Sea. AAPG bulletin 87, 909–934.

Colombera, L., Felletti, F., Mountney, N.P., McCaffrey, W.D., 2012. A database approach for constraining stochastic simulations of the sedimentary heterogeneity of fluvial reservoirs. AAPG Bulletin 96, 2143–2166. doi:10.1306/04211211179

Colomina, I., Molina, P., 2014. Unmanned aerial systems for photogrammetry and remote sensing: A review. ISPRS Journal of Photogrammetry and Remote Sensing 92, 79–97. doi:10.1016/j.isprsjprs.2014.02.013

Craig, L.C., Holmes, Cl.N., Cadigan, R.A., Freeman, V.L., Mullens, T.E., Weir, G.W., 1955. Stratigraphy of the Morrison and Related Formations, Colorado Plateau Region: A Preliminary Report. Geological Survey Bulletin 1009, 125–168.

Cuevas Martínez, J.L., Cabrera Pérez, L., Marcuello, A., Arbués Cazo, P., Marzo Carpio, M., Bellmunt, F., 2010. Exhumed channel sandstone networks within fluvial fan deposits from the Oligo-Miocene Caspe Formation, South-east Ebro Basin (North-east Spain). Sedimentology 57, 162–189. doi:10.1111/j.1365-3091.2009.01096.x

Currie, B.S., 1997. Sequence stratigraphy of nonmarine Jurassic – Cretaceous rocks , central Cordilleran foreland-basin system. Geological Society of America Bulletin 109, 1206–1222. doi:10.1130/0016-7606(1997)109<1206

DeCelles, P.G., Currie, B.S., 1996. Long-term sediment accumulation in the Middle Jurassic-early Eocene Cordilleran retroarc foreland-basin system. Geology 24, 591–594. doi:10.1130/0091-7613(1996)024<0591:LTSAIT>2.3.CO;2

DeCelles, P.G., Cavazza, W., 1999. A comparison of fluvial megafans in the Cordilleran (Upper Cretaceous) and modern Himalayan foreland basin systems. Bulletin of the Geological Society of America 111, 1315–1334. doi:10.1130/0016-7606(1999)111<1315:ACOFMI>2.3.CO;2

Demko, T.M., Currie, B.S., Nicoll, K.A., 2004. Regional paleoclimatic and stratigraphic implications of paleosols and fluvial/overbank architecture in the Morrison Formation (Upper Jurassic), Western Interior, USA. Sedimentary Geology 167, 115–135. doi:10.1016/j.sedgeo.2004.01.003

Dickinson, W.R., Gehrels, G.E., 2008. Sediment delivery to the Cordilleran foreland basin: Insights from U-Pb ages of detrital zircons in Upper Jurassic and Cretaceous strata of the Colorado Plateau. American Journal of Science 308, 1041–1082. doi:10.2475/10.2008.01

Dietrich, J.T., 2014. Application of Structure-from-Motion photogrammetry to fluvial geomorphology. Dissertation. University of Oregon.

Eisenbeiss, H., 2009. UAV Photogrammetry, Institute of Photogrammetry and Remote Sensing. doi:doi:10.3929/ethz-a-005939264

Enge, H.D., Buckley, S.J., Rotevatn, A., Howell, J.A., 2007. From outcrop to reservoir simulation model: Workflow and procedures. Geosphere 3, 469–490. doi:10.1130/GES00099.1

Ethridge, F.G., 2010. Interpretation of ancient fluvial channel deposits: Review and recommendations. From river to rock record: The preservation of fluvial sediments and their subsequent interpretation 9–36.

Favalli, M., Fornaciai, A., Isola, I., Tarquini, S., Nannipieri, L., 2012. Multiview 3D reconstruction in geosciences. Computers and Geosciences 44, 168–176. doi:10.1016/j.cageo.2011.09.012

Foix, N., Allard, J.O., Paredes, J.M., Giacosa, R.E., 2012. Fluvial styles, palaeohydrology and modern analogues of an exhumed, Cretaceous fluvial system: Cerro Barcino Formation, Cañadón Asfalto Basin, Argentina. Cretaceous Research 34, 298–307. doi:10.1016/j.cretres.2011.11.010

Fonstad, M.A., Dietrich, J.T., Courville, B.C., Jensen, J.L., Carbonneau, P.E., 2013. Topographic structure from motion: A new development in photogrammetric measurement. Earth Surface Processes and Landforms 38, 421–430. doi:10.1002/esp.3366

Furukawa, Y., Ponce, J., 2010. Accurate, Dense, and Robust Multi-View Stereopsis. IEEE Transactions on Pattern Analysis & Machine Intelligence 32, 1362–1376. doi:http://doi.ieeecomputersociety.org/10.1109/TPAMI.2009.161

Gawthorpe, R.L., Collier, R.E.L., Alexander, J., Bridge, J.S., Leeder, M.R., 1993. Ground penetrating radar: application to sandbody geometry and heterogeneity studies. Geological Society, London, Special Publications 73, 421–432. doi:10.1144/GSL.SP.1993.073.01.24

Gibling, M.R., 2006. Width and Thickness of Fluvial Channel Bodies and Valley Fills in the Geological Record: A Literature Compilation and Classification. Journal of Sedimentary Research 76, 731–770. doi:10.2110/jsr.2006.060

Gonçalves, J.A., Henriques, R., 2015. UAV photogrammetry for topographic monitoring of coastal areas. ISPRS Journal of Photogrammetry and Remote Sensing 104, 101–111. doi:10.1016/j.isprsjprs.2015.02.009

Hajek, E.A., Heller, P.L., Sheets, B.A., 2010. Significance of channel-belt clustering in alluvial basins. Geology 38, 535–538. doi:10.1130/G30783.1

Hardage, B.A., Levey, R.A., Pendleton, V., Simmons, J., Edson, R., 1994. A 3-D seismic case history evaluating fluvial deposited thin-bed reservoirs in a gas-producing property. Geophysics 59, 1650 LP-1665.

Hartley, A.J., Weissmann, G.S., Nichols, G.J., Warwick, G.L., 2010. Large Distributive Fluvial Systems: Characteristics, Distribution, and Controls on Development. Journal of Sedimentary Research 80, 167–183. doi:10.2110/jsr.2010.016

Hartley, A.J., Owen, A., Swan, A., Weissmann, G.S., Holzweber, B.I., Howell, J., Nichols, G., Scuderi, L., 2015. Recognition and importance of amalgamated sandy meander belts in the continental rock record. Geology 43, 679–682. doi:10.1130/G36743.1

Hasiotis, S.T., 2004. Reconnaissance of Upper Jurassic Morrison Formation ichnofossils, Rocky Mountain Region, USA: Paleoenvironmental, stratigraphic, and paleoclimatic significance of terrestrial and freshwater ichnocoenoses. Sedimentary Geology 167, 177–268. doi:10.1016/j.sedgeo.2004.01.006

Heller, P.L., Bowdler, S.S., Chambers, H.P., Coogan, J.C., Hagen, E.S., Shuster, M.W., Winslow, N.S., Lawton, T.F., 1986. Time of initial thrusting in the Sevier orogenic belt , Idaho-Wyoming and Utah Time of initial thrusting in the Sevier orogenic belt , Idaho-Wyoming and Utah. Geology 14, 388–391. doi:10.1130/0091-7613(1986)14<388

Hodgetts, D., 2013. Laser scanning and digital outcrop geology in the petroleum industry: A review. Marine and Petroleum Geology 46, 335–354. doi:10.1016/j.marpetgeo.2013.02.014

Horton, B.K., DeCelles, P.G., 1997. The modern foreland basin system adjacent to the Central Andes. Geology 25, 895–898. doi:10.1130/0091-7613(1997)025<0895:TMFBSA>2.3.CO;2

Horton, B.K., DeCelles, P.G., 2001. Modern and ancient fluvial megafans in the foreland basin system of the Central Andes, Southern Bolivia: Implications for drainage network evolution if foldthrust belts. Basin Research 13, 43–63. doi:10.1046/j.1365-2117.2001.00137.x

Hubbard, S.M., Fildani, A., Romans, B.W., Covault, J.A., McHargue, T.R., 2010. High-Relief Slope Clinoform Development: Insights from Outcrop, Magallanes Basin, Chile. Journal of Sedimentary Research 80, 357–375. doi:10.2110/jsr.2010.042

Ielpi, A., Ghinassi, M., 2014. Planform architecture, stratigraphic signature and morphodynamics of an exhumed Jurassic meander plain (Scalby Formation, Yorkshire, UK). Sedimentology 1923–1960. doi:10.1111/sed.12122

Iriondo, M., 1993. Geomoprhology and late Quaternary of the Chaco (South America). Geomorphology 289–303.

James, M.R., Robson, S., 2012. Straight forward reconstruction of 3D surfaces and topography with a camera: Accuracy and geoscience application. Journal of Geophysical Research: Earth Surface 117, 1–17. doi:10.1029/2011JF002289

James, M.R., Robson, S., 2014. Mitigating systematic error in topographic models derived from UAV and ground-based image networks. Earth Surface Processes and Landforms 1420, 1413–1420. doi:10.1002/esp.3609

Javernick, L., Brasington, J., Caruso, B., 2014. Modeling the topography of shallow braided rivers using Structure-from-Motion photogrammetry. Geomorphology 213, 166–182. doi:10.1016/j.geomorph.2014.01.006

Jones, L.S., Gustason, E.R., 2006. Dinosaurs as Possible Avulsion Enablers in the Upper Jurassic Morrison Formation, East-Central Utah. Ichnos 13, 31–41. doi:10.1080/10420940500516370

Kjemperud, A. V., Schomacker, E.R., Cross, T.A., 2008. Architecture and stratigraphy of alluvial deposits, Morrison Formation (Upper Jurassic), Utah. AAPG Bulletin 92, 1055–1076. doi:10.1306/03250807115

Latrubesse, E.M., Stevaux, J.C., Cremon, E.H., May, J.H., Tatumi, S.H., Hurtado, M.A., Bezada, M., Argollo, J.B., 2012. Late Quaternary megafans, fans and fluvio-aeolian interactions in the Bolivian Chaco, Tropical South America. Palaeogeography, Palaeoclimatology, Palaeoecology 356–357, 75–88. doi:10.1016/j.palaeo.2012.04.003

Leier, A.L., DeCelles, P.G., Pelletier, J.D., 2005. Mountains, monsoons, and megafans. Geology 33, 289–292. doi:10.1130/G21228.1

Leopold, L.B., Wolman, M.G., 1960. River Meanders. Bulletin of the Geological Society of America 71, 769–794. doi:10.1130/0016-7606(1960)71[769:RM]2.0.CO;2

Long, N., Millescamps, B., Guillot, B., Pouget, F., Bertin, X., 2016. Monitoring the Topography of a Dynamic Tidal Inlet Using UAV Imagery. Remote Sensing 8, 387. doi:10.3390/rs8050387

Lowe, D.G., 1999. Object Recognition from Local Scale-Invariant Features. IEEE International Conference on Computer Vision 1150–1157. doi:10.1109/ICCV.1999.790410

Lowe, D.G., 2004. Distinctive image features from scale-invariant keypoints. International Journal of Computer Vision 60, 91–110. doi:10.1023/B:VISI.0000029664.99615.94

Mancini, F., Dubbini, M., Gattelli, M., Stecchi, F., Fabbri, S., Gabbianelli, G., 2013. Using unmanned aerial vehicles (UAV) for high-resolution reconstruction of topography: The structure from motion approach on coastal environments. Remote Sensing 5, 6880–6898. doi:10.3390/rs5126880

Martinez, J.F., Cartwright, J.A., Burgess, P.M., Bravo, J.V., 2004. 3D Seismic Interpretation of the Messinian Unconformity in the Valencia Basin, Spain. Geological Society, London, Memoirs 29, 91–100. doi:10.1144/GSL.MEM.2004.029.01.10

Martinius, A.W., Naess, A., 2005. Uncertainty analysis of fluvial outcrop data for stochastic reservoir modelling. Petroleum Geoscience 11, 203–214. doi:10.1144/1354-079303-615

McGlue, M.M., Smith, P.H., Zani, H., Silva, A., Carrapa, B., Cohen, A.S., Pepper, M.B., 2016. An Integrated Sedimentary Systems Analysis of the Io Bermejo (Argentina): Megafan Character in the Overfilled Southern Chaco Foreland Basin. Journal of Sedimentary Research 86, 1359–1377. doi:10.2110/jsr.2016.82

Miall, A.D., 1985. Architectural-element analysis: A new method of facies analysis applied to fluvial deposits. Earth-Science Reviews 22, 261–308. doi:10.1016/0012-8252(85)90001-7

Miall, A.D., 1996. The geology of fluvial deposits: sedimentary facies, basin analysis, and petroleum geology, The geology of fluvial deposits: sedimentary facies, basin analysis, and petroleum geology.

Miall, A.D., 2006. Reconstructing the architecture and sequence stratigraphy of the preserved fluvial record as a tool for reservoir development: A reality check. AAPG Bulletin 90, 989–1002. doi:10.1306/02220605065

Micheletti, N., Chandler, J.H., Lane, S.N., 2014. Investigating the geomorphological potential of freely available and accessible structure-from-motion photogrammetry using a smartphone. Earth Surface Processes and Landforms 40, 473–486. doi:10.1002/esp.3648

Moody-Stuart, M., 1966. High- and low-sinuosity stream deposits, with examples from the Devonian of Spitsbergen. Journal of Sedimentary Petrology 36, 1102–1117.

Mullens, T., Freeman, V.L., 1957. Lithofacies of the Salt Wash Member of the Morrison Formation, Colorado Plateau. Geological Society of America Bulletin 68, 605–626.

Myers, T.S., Tabor, N.J., Rosenau, N.A., 2014. Multiproxy approach reveals evidence of highly variable paleoprecipitation in the Upper Jurassic Morrison Formation (western United States). Bulletin of the Geological Society of America 126, 1105–1116. doi:10.1130/B30941.1

Nex, F., Remondino, F., 2014. UAV for 3D mapping applications: A review. Applied Geomatics 6, 1–15. doi:10.1007/s12518-013-0120-x

Nichols, G.J., Fisher, J.A., 2007. Processes, facies and architecture of fluvial distributary system deposits. Sedimentary Geology 195, 75–90. doi:10.1016/j.sedgeo.2006.07.004

Niethammer, U., James, M.R., Rothmund, S., Travelletti, J., Joswig, M., 2012. UAV-based remote sensing of the Super-Sauze landslide: Evaluation and results. Engineering Geology 128, 2–11. doi:10.1016/j.enggeo.2011.03.012

Owen, A., Jupp, P.E., Nichols, G.J., Hartley, A.J., Weissmann, G.S., Sadykova, D., 2015a. Statistical estimation of the position of an apex: application to the geological record. Journal of Sedimentary Research 85, 142–152. doi:http://dx.doi.org/10.2110/jsr.2015.16

Owen, A., Nichols, G.J., Hartley, A.J., Weissmann, G.S., 2015b. Vertical trends within the prograding Salt Wash distributive fluvial system, SW United States. Basin Research 1–17. doi:10.1111/bre.12165

Owen, A., Nichols, G.J., Hartley, A.J., Weissmann, G.S., Scuderi, L.A., 2015c. Quantification of a distributive fluvial system: the Salt Wash DFS of the Morrison. SEPM Journal of Sedimentary Research 85, 544–561. doi:10.2110/jsr.2015.35

Parrish, J.T., Peterson, F., Turner, C.E., 2004. Jurassic “savannah” - Plant taphonomy and climate of the Morrison Formation (Upper Jurassic, Western USA). Sedimentary Geology 167, 137–162. doi:10.1016/j.sedgeo.2004.01.004

Pemberton, E.A.L., Hubbard, S.M., Fildani, A., Romans, B., Stright, L., 2016. The stratigraphic expression of decreasing confinement along a deep-water sediment routing system: Outcrop example from southern Chile. Geosphere 12, 114–134. doi:10.1130/GES01233.1

Peterson, F., 1980. Sedimentology of the uranium-bearing Salt Wash Member and Tidwell unit of the Morrison Formation in the Henry and Kaiparowits basins, Utah, in: Picard, M.D. (Ed.), Henry Mountains Symposium. Utah Geological Association Publication, pp. 305–322.

Peterson, F., 1984. Fluvial sedimentation on a quivering craton: influence of slight crustal movements on fluvial processes, Upper Jurassic Morrison Formation, western Colorado Plateau. Sedimentary Geology 38, 21–49.

Rarity, F., van Lanen, X.M.T., Hodgetts, D., Gawthorpe, R.L., Wilson, P., Fabuel-Perez, I., Redfern, J., 2013. LiDAR-based digital outcrops for sedimentological analysis: workflows and techniques. Geological Society, London, Special Publications 387, 153–183. doi:10.1144/SP387.5

Rittersbacher, A., Buckley, S.J., Howell, J. a., Hampson, G.J., Vallet, J., 2013. Helicopter-based laser scanning: a method for quantitative analysis of large-scale sedimentary architecture. Geological Society, London, Special Publications 387, 185–202. doi:10.1144/SP387.3

Robinson, J.W., McCabe, P.J., 1997. Sandstone-body and shale-body dimensions in a braided fluvial system: Salt wash sandstone member (Morrison formation), Garfield County, Utah. AAPG Bulletin 81, 1267–1291. doi:10.1306/522B4DD9-1727-11D7-8645000102C1865D

Robinson, J.W., McCabe, P.J., 1998. Evolution of a braided river system: the Salt Wash member of the Morrison Formation (Jurassic) in southern Utah, in: Relative Role of Eustasy, Climate, and Tectonism in Continental Rocks. pp. 93–108.

Rust, G.L., Weissmann, G.S., Werban, U., Frechette, J.D., Wawrzyniec, T.F., 2011. Outcrop-Based GPR Tomography Through Braided-Stream Deposits, in: Martinsen, O.J., Pulham, A.J., Haughton, P., Sullivan, M.D. (Eds.), Outcrops Revitalized: Tools, Techniques and Applications. SEPM (Society for Sedimentary Geology), pp. 227–238. doi:10.2110/sepmcsp.10.227

Ryan, J.C., Hubbard, A.L., Todd, J., Carr, J.R., Box, J.E., Christoffersen, P., Holt, T.O., Snooke, N., 2015. UAV photogrammetry to assess calving front dynamics at a large outlet glacier draining the Greenland Ice Sheet. The Cryosphere Discussions 8, 2243–2275. doi:10.5194/tcd-8-2243-2014

Shortis, M.R., Bellman, C.J., Robson, S., Johnston, G.J., Johnson, G.W., 2006. Stability of Zoom and Fixed Lenses used with Digital SLR Cameras. International Archives of Photogrammetry, Remote Sensing, and Spatial Information Sciences 36, 285–290.

Siebert, S., Teizer, J., 2014. Mobile 3D mapping for surveying earthwork projects using an Unmanned Aerial Vehicle (UAV) system. Automation in Construction 41, 1–14. doi:10.1016/j.autcon.2014.01.004

Singh, H., Parkash, B., Gohain, K., 1993. Facies analysis of the Kosi megafan deposits. Sedimentary Geology 85, 87–113. doi:10.1016/0037-0738(93)90077-I

Snavely, N., Seitz, S.M., Szeliski, R., 2006. Photo Tourism: Exploring Photo Collections in 3D. ACM Transactions on Graphics 25, 835–846. doi:10.1145/1141911.1141964

Snavely, N., Seitz, S.M., Szeliski, R., 2008. Modeling the world from Internet photo collections. International Journal of Computer Vision 80, 189–210. doi:10.1007/s11263-007-0107-3

Tang, L., Braun, J., Debitsch, R., 1997. Automatic aerotriangulation—concept, realization and results. ISPRS journal of photogrammetry and remote sensing 52, 122–131.

Triggs, B., McLauchlan, P.F., Hartley, R.I., Fitzgibbon, A.W., 2000. Bundle Adjustment—A Modern Synthesis, in: Triggs, B., Zisserman, A., Szeliski, R. (Eds.), Vision Algorithms: Theory and Practice. Springer Berlin Heidelberg, Berlin, Heidelberg, pp. 298–372. doi:10.1007/3-540-44480-7_21

Turner, C.E., Peterson, F., 2004. Reconstruction of the Upper Jurassic Morrison Formation extinct ecosystem—a synthesis. Sedimentary Geology 167, 309–355. doi:10.1016/j.sedgeo.2004.01.009

Turner, D., Lucieer, A., Wallace, L., 2014. Direct georeferencing of ultrahigh-resolution UAV imagery. IEEE Transactions on Geoscience and Remote Sensing 52, 2738–2745. doi:10.1109/TGRS.2013.2265295

Tyler, N., Ethridge, F., 1983. Depositional Setting of the Salt Wash Member of the Morrison Formation, Southwest Colorado. SEPM Journal of Sedimentary Research Vol. 53, 67–82. doi:10.1306/212F8157-2B24-11D7-8648000102C1865D

Weber, K.J., 1992. The Use of 3-D Seismic in Reservoir Geological Modelling, in: The Geological Modelling of Hydrocarbon Reservoirs and Outcrop Analogues. Blackwell Publishing Ltd., pp. 181–188. doi:10.1002/9781444303957.ch11

Weissmann, G.S., Hartley, A.J., Nichols, G.J., Scuderi, L.A., Olson, M., Buehler, H., Banteah, R., 2010. Fluvial form in modern continental sedimentary basins: Distributive fluvial systems. Geology 38, 39–42. doi:10.1130/G30242.1

Weissmann, G.S., Hartley, A.J., Nichols, G.J., Scuderi, L.A., Olson, M.E., 2011. Alluvial facies distributions in continental sedimentary basins-distributive fluvial systems, in: From River to Rock Record: The Preservation of Fluvial Sediments and Their Subsequent Interpretation. SEPM, pp. 327–355.

Weissmann, G.S., Hartley, A.J., Ab, A., Scuderi, L. a, Nichols, G.J., Davidson, S.K., Owen, A., Atchley, S.C., Bhattacharyya, P., Michel, L., Tabor, N.J., 2013. Prograding distributive fluvial systems - geomorphic models and ancient examples. SEPM Sepecial Pulication 131–147. doi:10.2110/sepmsp.104.16

Weissmann, G.S., Hartley, A.J., Scuderi, L.A., Nichols, G.J., Owen, A., Wright, S., Felicia, A.L., Holland, F., Anaya, F.M.L., 2015. Fluvial geomorphic elements in modern sedimentary basins and their potential preservation in the rock record: A review. Geomorphology 250, 187–219. doi:10.1016/j.geomorph.2015.09.005

Westoby, M.J., Brasington, J., Glasser, N.F., Hambrey, M.J., Reynolds, J.M., 2012. “Structure-from-Motion” photogrammetry: A low-cost, effective tool for geoscience applications. Geomorphology 179, 300–314. doi:10.1016/j.geomorph.2012.08.021

Wilkinson, M.W., Jones, R.R., Woods, C.E., Gilment, S.R., McCaffrey, K.J.W., Kokkalas, S., Long, J.J., 2016. A comparison of terrestrial laser scanning and structure-from-motion photogrammetry as methods for digital outcrop acquisition. Geosphere 12, 1–16. doi:10.1130/GES01342.1

Wu, C., 2013. Towards linear-time incremental structure from motion. Proceedings - 2013 International Conference on 3D Vision, 3DV 2013 127–134. doi:10.1109/3DV.2013.25

Wu, C., Bhattacharya, J.P., 2015. Paleohydrology and 3D Facies Architecture of Ancient Point Bars , Ferron Sandstone, Notom Delta, South-central Utah. Journal of Sedimentary Research 399–418. doi:10.2110/jsr.2015.29

APPENDIX A

UAV-SFM ACCURACY ASSESSMENT

Images were collected using an autonomous, fixed-wing, UAV (eBee, from Sensefly) that carried an 18.2 MP digital camera (Sony) with a 25 mm focal length lens. The UAV is equipped with an on-board artificial intelligence system that analyzes data from an Inertial Measurement Unit and an on-board GPS to optimize the flight. The images were processed using Pix4Dmapper (Pix4D) photogrammetry-software.

Data were collected from open fields in Columbia, South Carolina, USA (Fig. A.1A). We acquired images with an 80% lateral and longitudinal overlap and a flight altitude of 120 m (394 feet) above the local surface. In total, 78 images were taken covering roughly 0.18 km^2, and requiring a flight time of approximately 10 minutes. GCPs (n = 9) were collected using a RTK differential GPS (Trimble R8) system to obtain absolute coordinates one and two centimeter-level accuracy in the horizontal and vertical, respectively and GCPs yielded a mean accuracy of 0.009 and 0.013 m in the horizontal and vertical, respectively. The images were geotagged with the UAVs onboard GPS unit with a mean horizontal accuracy of 1.96 m and a vertical accuracy of 2.61 m. Static features (n = 51) were measured on the ground using a tape measure to provide ground-truth data to compare with the SfM model.

To evaluate relative and absolute accuracy the dataset was processed in the SfM software twice: once with GCPs, the other without GCPs (non-GCP). The summary of both datasets can be seen in table A.1. The GCPs were used to scale and georeference one of the datasets, which yielded a RMS error of 0.053 m. The total processing time took between 1 and 2 hours and resulted in a dense point-cloud, DSM, and orthomosaic (Fig. A.1B-C).

The absolute accuracy was assessed by comparing the amount of horizontal and vertical shift between the SfM outputs from the GCP and non-GCP datasets (Fig. A.2A-C). Based on the difference between the two datasets, there was an average shift of 1.24 m in the horizontal and 3.47 m in the vertical. The horizontal shift was determined by picking features between both datasets and then calculating the distance between those corresponding features. The degree of horizontal offset varied across the orthomosaic, with an average of 0.66 m in the western portion of the study area and 1.63 m in the eastern region (Fig. A.2A). The vertical shift was determined by subtracting both DSMs to calculate the change in elevation. The vertical offset saw a wide range from -18.34 m to 29.71 m (Fig. A.2B). However, those extremes are focused in areas with vertical structures or bodies of water. The mean was found to be 3.47 m with a standard deviation of 2.09 m (Fig. A.2C).

The internal accuracy was assessed by comparing corresponding measurements from the ground with both datasets (GCP and non-GCP). In order to assess the internal accuracy, static features (n = 51) measured on the ground were compared with measurements digitized on the produced orthomosaics in

order to determine if there is a statistically significant difference. The data was compared using a one-way analysis of variance (ANOVA) test, which demonstrated no statistically significant difference between the mean of the measured groups ($F(2,150) = 0.000294$, $p = 0.999706$, Table A.2). This indicates that measurements within the non-GCP dataset (with geotagged imagery) were statistically equal to those on the ground and in the GCP dataset, thereby demonstrating a high degree of internal accuracy in non-GCP dataset constructed from geotagged imagery.

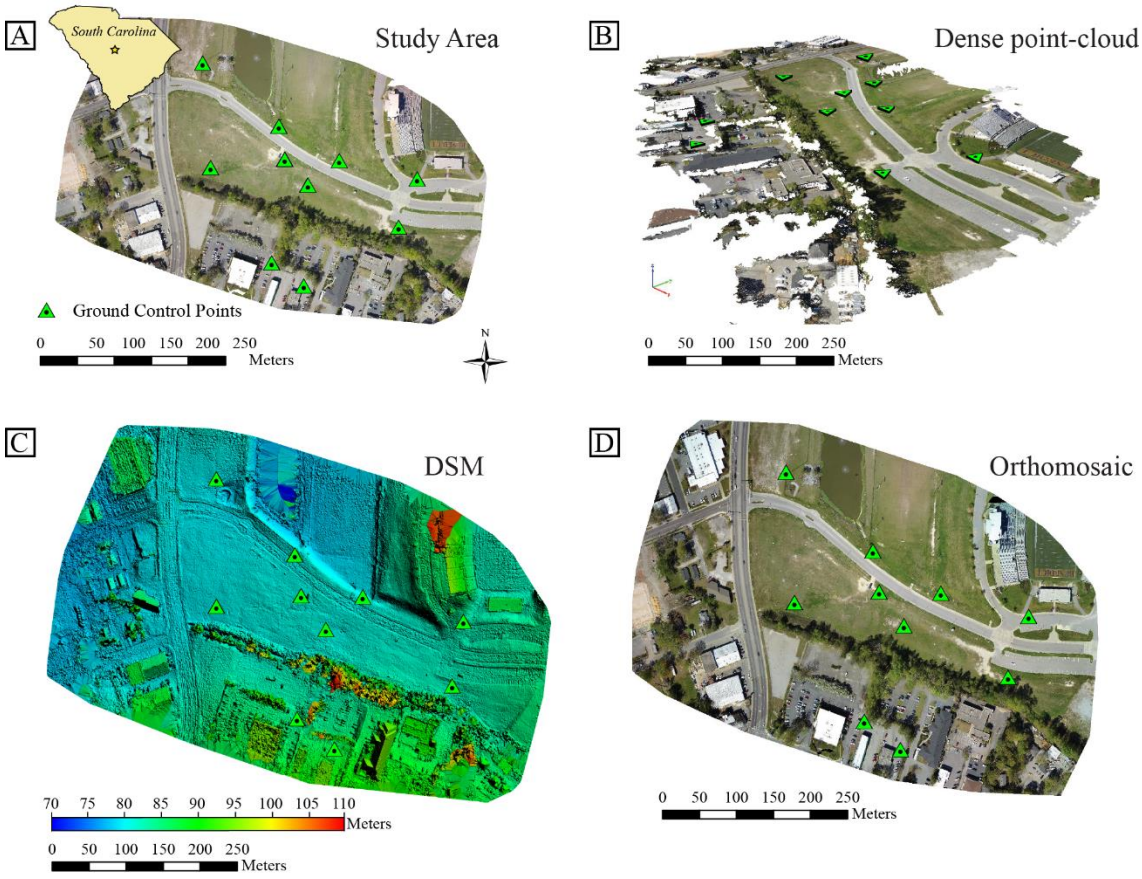

Figure A.1. A) Study area near the University of South Carolina. The green triangles represent the distribution for ground control points (GCPs) and are appropriately placed on the other images (B-D) as a reference. B) A perspective view of the study area taken from the densified point-cloud. C) The DSM and orthomosaic (D) are the last to be generated during processing.

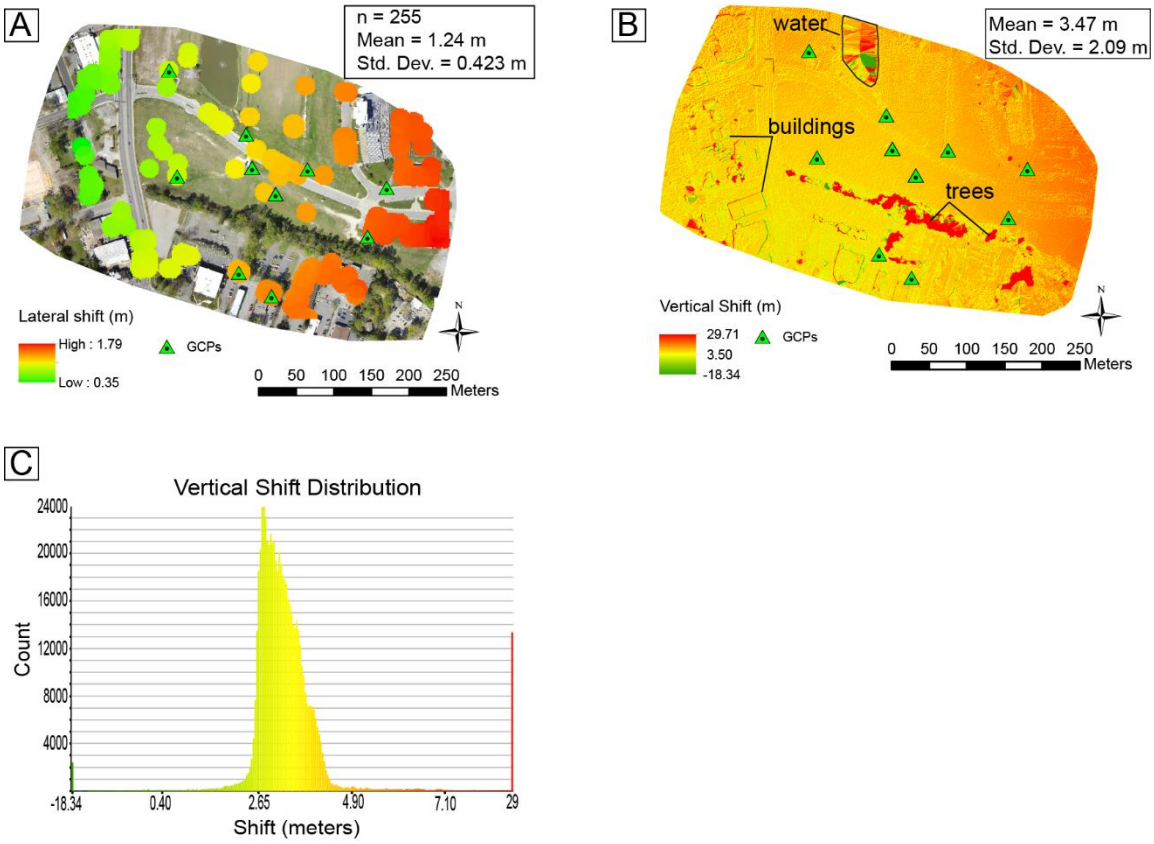

Figure A.2. Absolute accuracy of the UAV-SfM reconstructions by comparing the lateral and vertical location of the dataset with and without GCPs. The green triangles represent the locations of the ground control points. A) The degree of lateral shift was determined by manually picking identical features in both datasets and then computing the distance between corresponding points. Red indicates a large shift while green indicates only a small amount of shift. It is apparent from this figure that the degree of shift is not evenly distributed across the dataset. B) The two digital surface models (DSMs) where subtracted from each other using the map algebra tool in ArcMap (10.3) to determine the degree of vertical shift in absolute space. It's worthwhile to note the extremes (-18.34 and 29.71) are positioned in areas with vertical structures (e.g. trees) and bodies of water while the majority of the DSM shows a vertical shift of about 3.47 m. C) Histogram showing the distribution of vertical shift. The average difference is 3.46 m with a standard deviation of 2.09 m.

Table A.1. Summary of the datasets used in the accuracy assessment and case study.

	ACCURACY ASSESSMENT		CASE STUDY
	GCPs	**No GCPs**	
AREA (KM^2)	0.1846	0.1846	0.8735
ALTITUDE	120	120	92
TIME FOR DATA CAPTURE (MINS)	8.2	8.2	32.37
NUMBER OF IMAGES	78	78	516
PROCESSING TIME (MINS)			
INITIAL PROCESSING	17.5	14.67	68.42
POINT-CLOUD DESIFICATION	26.1	29.34	154.17
DSM AND ORTHOMOSAIC GENERATION	23.15	55.65	119.47
TOTAL	66.75	99.66	342.06
MEDIAN KEYPOINTS PER IMAGE	46,220	46,220	63,362
MEDIAN MATCHES PER IMAGE	19,634.8	18,231.4	15,037.7
NUMBER OF 3-D DENSIFIED POINTS	10,839,906	10,777,816	71,977,263
AVERAGE POINT DENSITY (PER M^3)	79.1	79.43	117
AVERAGE GROUND RESOLUTION (CM/PIXEL)	3.36	3.35	2.68

Table A.2. Results from the one-way ANOVA test.

	N	*Sum*	*Mean*	*Std. Dev.*	*Min.*	*Max.*	*Variance*
GCP	51	409.7	8.0	15.7	1.5	85.2	245.2
Non GCP	51	408.7	8.0	15.6	1.5	85.1	244.3
Ground	51	412.6	8.1	15.6	1.5	84.8	243.4

	Sum of Squares	*df*	*Mean Square*	*F*	*P-value*
Between Groups	0.1438004	2	0.0719	0.000294	0.999706
Within Groups	36641.0345	150	244.2736		

df = degree of freedom; F = variation between sample means; P-value = probability the data from all groups have identical means